

**DESIGN AND FABRICATION OF DISPERSION-ENGINEERED PHOTONIC
CRYSTALS FOR APPLICATIONS IN THE MICROWAVE REGIME**

by

Jerico N. Sabas

A thesis submitted to the Faculty of the University of Delaware in partial fulfillment of the requirements for the degree of Master of Science in Electrical and Computer Engineering

Summer 2010

Copyright © 2010 Jerico N. Sabas
All Rights Reserved

**DESIGN AND FABRICATION OF DISPERSION-ENGINEERED PHOTONIC
CRYSTALS FOR APPLICATIONS IN THE MICROWAVE REGIME**

by
Jerico N. Sabas

Approved: _____
Dennis W. Prather, Ph.D.
Professor in charge of thesis on behalf of the Advisory Committee

Approved: _____
Kenneth Barner, Ph.D.
Chair of the Department of Electrical and Computer Engineering

Approved: _____
Michael J. Chajes, Ph.D.
Dean of the College of Engineering

Approved: _____
Debra Hess Norris, M.S.
Vice Provost for Graduate and Professional Education

ACKNOWLEDGMENTS

The research presented in this thesis is, of course, a result of joint collaborative efforts. There are several people to whom I must express my sincerest appreciation, for, without their support, this research would have been impossible. First, I would like to thank my advisor, Dr. Dennis W. Prather, for his persistent support and encouragement that have brought me to this point in my professional career. He has always provided us with the necessary funding and first-class facilities that are conducive to successful research. In leading the research group, Dr. Prather demonstrates an optimism, determination, and work ethic that inspire us all.

I would like to acknowledge Dr. Steve Russell from the Office of Naval Research (ONR) for supporting this effort.

I would like to extend my gratitude to all the colleagues and mentors in our research group for their support and consideration that have made this research possible. They have made my time as a member of this group productive and entertaining. I particularly want to thank Dr. Shouyuan Shi, who has been the intellectual leader of this research effort and has always made himself available to listen to new ideas and to offer advice. Thanks to Dr. Iftekhar Mirza who took me under his wing when I first joined the group and has since participated in every aspect of this research.

Finally, I would like to thank my family, for their support that helped to keep me in track and filled me with confidence when it seemed impossible to reach

this objective. To my mother and father, thanks so much for motivating me to pursue this path and for their efforts that made it all possible. Most importantly I want to thank my wife, for her support and understanding throughout the length of this research. Thank you for your love and kindness and for being there always for me.

TABLE OF CONTENTS

LIST OF TABLES	vii
LIST OF FIGURES	viii
ABSTRACT	xi
1 INTRODUCTION	1
1.1 A Brief Introduction to Photonic Crystals	1
1.2 Historical Overview	3
1.3 Theoretical Background	4
1.4 Research Motivation and Thesis Outline	9
2 ANALYSIS OF PHOTONIC CRYSTAL STRUCTURES	12
2.1 Introduction	12
2.2 Photonic Bandgap Structures	13
2.2.1 Point Defect Implantation.....	14
2.2.2 Line Defect Line Implantation	14
2.3 Dispersion Engineered Photonic Crystals	16
3 SELF-COLLIMATION OF LIGHT IN 2D LOW INDEX CONTRAST (LIC) PHOTONIC CRYSTALS	22
3.1 Design of 2D LIC SCPhC	23
3.2 Numerical Characterization of LIC SCPhC	27
3.3 Fabrication of LIC SCPhC	29
3.4 Experimental Demonstration of Self-Collimation in 2D LIC PhC	30
3.5 Experimental Verification of Transmission Efficiency in LIC SCPhCs.....	32
3.6 Discussion and Conclusions	35
4 HIGH INDEX CONTRAST (HIC) SELF-COLLIMATING PHOTONIC CRYSTAL.....	37
4.1 Design of 2D HIC SCPhC.....	37
4.2 Numerical Characterization of HIC SCPhC.....	40
4.3 Fabrication of HIC SCPhC.....	43

4.4	Experimental Demonstration of Self-Collimation in HIC PhC.....	44
4.5	Experimental Verification of Transmission Efficiency in HIC SCPhC.....	46
5	COAXIAL-TO-PHC COUPLING FOR INTEGRATION IN THE MICROWAVE REGIME.....	50
5.1	Introduction	50
5.2	Coupler Design.....	50
5.3	Numerical Characterization of Coupler.....	52
5.4	Fabrication of I/O Coupler	53
5.5	Experimental Verification of Coupler Efficiency	54
6	CONCLUSIONS AND FUTURE WORK.....	58
6.1	Conclusions	58
6.2	Future Work.....	59
	REFERENCES.....	61

LIST OF TABLES

Table 4.1	Transmission loss data for HIC and LIC PhC slabs of different length.	49
-----------	--	----

LIST OF FIGURES

Figure 1.1	Dispersion diagram for a PhC with a photonic bandgap.....	7
Figure 1.2	Dispersion surface and equifrequency contours for a square-lattice PhC..	8
Figure 2.1	PBG material with implanted line defect,(a) graphical illustration of the structure, and (b) FDTD simulation of guided waves within the defect line.....	15
Figure 2.2	(a) Dispersion surfaces for a natural homogeneous material, (b) 2D dispersion diagram for a PBG material, (c) dispersion surface for a triangular-lattice PhC, and (d) dispersion surface for a square lattice PhC.....	18
Figure 2.3	FDTD simulation of an electromagnetic light wave emanating from a point source when placed in a (a) homogeneous (unpatterned) silicon slab and (b) a silicon slab perforated with a square lattice of air holes..	21
Figure 3.1	Illustration of a square-lattice PhC with its physical design parameters.	23
Figure 3.2	First band dispersion equifrequency contours for LIC SCPhC.....	25
Figure 3.3	(a) First band dispersion surface of a PhC, and (b) equifrequency contours for our SCPhC design for $a = 0.45\lambda$	26
Figure 3.4	Simulated LIC SCPhC and its electric field distribution captured at 12 GHz.	28
Figure 3.5	Simulated SCPhC with shifted I/O couplers and its electric field distribution at 12 GHz.....	29
Figure 3.6	Simulated electric field distribution for out-of-plane scattering for LIC SCPhC.....	29

Figure 3.7	Fabricated SCPPhC connected to I/O couplers for experimental measurement of transmission efficiency.	30
Figure 3.8	Experimental setup for 2D scanning of SCPPhC.	31
Figure 3.9	Measured electric field distribution for 12-inch LIC PhC (a) amplitude, and (b) phase.	32
Figure 3.10	Numerical and experimental results for insertion loss for LIC SCPPhC.	33
Figure 3.11	Measured transmission loss for different length slabs for LIC PhC.	35
Figure 4.1	(a) 3D EFCs for $a = 0.36\lambda$ for HIC SCPPhC, and (b) equivalent 2D EFCs for HIC PhC.	38
Figure 4.2	EFC of HIC SCPPhC for $a = 0.36\lambda$, showing the spatial angle for self-collimation.	40
Figure 4.3	Simulation setup for HIC PhC.	41
Figure 4.4	FDTD simulation of electric field distribution for HIC PhC captured at 10.1 GHz.	42
Figure 4.5	Numerical results for insertion loss for FDTD simulation of HIC PhC at 10.1 GHz.	43
Figure 4.6	Fabrication components for HIC PhC.	44
Figure 4.7	Measured electric field distribution amplitude and phase fronts for HIC PhC for (a) 12 inch slab, and (b) 18 inch slab.	45
Figure 4.8	Transmission loss comparison between HIC and LIC PhC.	47
Figure 4.9	Measured transmission loss for different length slabs of HIC PhC.	48
Figure 5.1	Electric field distribution for I/O couplers at 12 GHz.	52
Figure 5.2	Numerical results for back-to-back I/O couplers.	53
Figure 5.3	Dielectric transitions.	54

Figure 5.4	Fabricated I/O coupler.....	54
Figure 5.5	Comparison of experimental and numerical results for back-to-back I/O couplers	55
Figure 5.6	Graphical notion of transmission loss components.....	55
Figure 5.7	Impedance mismatch loss calculation through linear extrapolation of the transmission data for different-length PhCs, (a) for LIC PhC, and (b) for HIC PhC	56
Figure 6.1	Illustrations for proposed methods to improve impedance matching between I/O couplers and PhCs (a) by optimizing the dimensions of the dielectric horn, and (b) by designing an effective index coupler.	60

ABSTRACT

The limitations facing electronics integrated circuits have placed an imminent wall for the progression of computational speeds and bandwidth, opening the door for research of the optical properties of materials. Photonic crystals (PhCs) are projected as the fundamental platform for the development of photonic integration. These PhCs provide novel approaches to control the propagation of light using dielectric structures that can be scaled down to nanometer dimensions for near infrared (NIR) or visible light applications, or scaled up for microwave or millimeter-wave applications. The initial interest in PhCs arose from the discovery of a photonic bandgap that made them suitable for a variety of applications. The possibilities of PhCs were further expanded with the understanding of the unique dispersion properties of PhCs. This thesis is concerned with a particular dispersion property of PhCs that permits the propagation of a beam of light through the PhC without divergence despite the fact that no physical route is introduced; this dispersion property is fittingly identified as self-collimation.

We engineered the dispersion properties of 2D periodic structures composed of dielectric rods to demonstrate, numerically and experimentally, the existence of self-collimation in PhCs in the microwave frequency regime. We designed and fabricated a low-index-contrast (LIC) PhC and experimentally demonstrated self-collimation, both in amplitude and phase, and measured the transmission efficiency for the LIC PhC slab. These results achieved for LIC PhCs provided principal insights into self-collimation that allowed us to extend our work to

a high-index-contrast (HIC) PhC design to improve the confinement of light within the PhC. We designed, numerical simulated, and fabricated a PhC made with high-index ceramic rods and experimentally demonstrated a significant improvement in self-collimation compared to the LIC PhC. In particular, we addressed the issue of coupling the PhC to a coaxial medium by designing an input/output (I/O) coupler. We fabricated this coupler as a hybrid of commercially-available and original components and experimentally characterized the coupling efficiency with both the LIC and HIC PhCs.

Chapter 1

INTRODUCTION

1.1 A Brief Introduction to Photonic Crystals

Within the last century, technology has been developed that allowed us to control the electrical properties of materials. Subsequently, advances in the field of semiconductor physics brought the discovery of the pn junction and the transistor, resulting in the invention of the integrated circuit (IC), which revolutionized the field of electronics and produced immeasurable changes in our society. For the next four decades, the performance of electronic integrated circuits (ICs) advanced exponentially, in terms of density and speed. However, due to the great complexity achieved with time, this technology has recently faced limitations in bandwidth, computational speeds and power consumption due to factors such as heat buildup and resistance-capacitance (RC) delays that are characteristic to metallic materials that make up the wires and interconnects of current electronic ICs. Extensive resources have been devoted to the research for a solution to these limitations since the present IC technologies based on metallic wires are projected to plateau at speeds around 10 GHz [1], which at the current pace would occur within a decade. The research suggests that in the near future the advancement in IC performance is expected to be driven by the invention of high temperature superconductors made of ceramics and alloys and the design of optical devices and artificial materials with enhanced electrical properties [2].

In recent decades, there has been significant research activity in the manipulation of the optical properties of materials. The goal of such research is to design photonic devices to generate, transmit, and process data at high speeds and over broad bandwidths for the current and future generations of communications systems, both for on-chip applications and telecommunications. A simple example is fiber optics technology, which has revolutionized the telecommunications industry by merely guiding light more efficiently than preceding technologies. The design of photonic devices that can efficiently control light waves over a desired range of frequencies by reflecting them, transmitting them only in a particular direction or confining them within a specific volume would enable significant technological developments. With these goals in mind, we performed the research into photonic crystals (PhCs) that is presented in this thesis.

A photonic crystal (PhC) can be generally defined as a periodic structure of optical, dielectric materials [3]; they are often artificial materials consisting of a periodic arrangement of structures whose electrical properties are different to those of the host material. For this reason, PhCs are said to be analogous to naturally-occurring semiconductor crystals which have a periodic structure in the atomic scale. PhCs can be designed to possess a photonic bandgap (PBG) for certain frequencies in the electromagnetic spectrum, in much the same way as electronic bandgaps in semiconductor materials. Additionally, as crystalline semiconductor materials were the basis for large-scale integration of electronic components, PhCs are expected to become the foundation for large-scale photonic integrated circuits. Since photonic technology lags around 30 years behind current semiconductor technology in terms of integration and maturity, the basic idea is to develop artificial photonic crystals with a

special dielectric pattern that can respond to photons similar to the way that ordinary semiconductor crystals respond to electrons.

1.2 Historical Overview

The history of artificial PhCs can be traced back to Lord Rayleigh's invention of gratings in 1887. It took nearly a century for the next significant development in the field, when Bykov proposed a 1D thin film periodic structure to suppress specific electronic frequencies [3]. Nonetheless, the current interest in PhCs arose from the theoretical papers by Eli Yablonovitch [4] and Sajeev John [5] in 1987, where they proposed that a periodic dielectric structure can have the property of photonic bandgap (PBG) for certain regions in the electromagnetic spectrum, analogous to electronic bandgaps that exist in semiconductor materials. Based on these theoretical assertions, various researchers unsuccessfully attempted to demonstrate a photonic bandgap experimentally based on a face-centered-cubic (FCC) lattice. Subsequently, Soukoulis [6] proposed and demonstrated a complete bandgap by fabricating a diamond lattice with dielectric spheres; later, Yablonovitch fabricated a diamond structure by drilling cylindrical holes on a planar dielectric slab and found a complete bandgap. The woodpile structure was then invented and became the first 3D photonic crystal, but their applications were limited due to the inflexibility of their designs and the difficulty of introducing defects [3].

Based on the success of the early work, photonic crystals earned the attention of many researchers and engineers in the photonics and optics communities, and due to this popularity, photonic bandgap (PBG) materials became synonymous with "photonic crystals". In particular, the two-dimensional PhCs became the center of

this research due to the simplicity of their fabrication and analysis. As a result, many optical devices were designed based on 2D PhCs, that is, 2D PBGs. These 2D PBGs were introduced by Joannopoulos et al. [2] and can be realized with a periodic array of dielectric rods or a periodic array of air holes on a dielectric slab. Optical switches and micro lasers were only a couple of the early applications found for PBGs. It was found that introducing defects to the PBG could be useful for subwavelength applications. For instance, by introducing a point defect in the PBG material, a high- Q microcavity can be formed; furthermore, a channel drop filter can be designed by incorporating multiple cavities tuned for different frequencies on a single PBG. Also, by incorporating line defects into a PBG material, the device can act as a dielectric waveguide that propagates light within confined path. Another significant result of the research on PBG materials was the discovery of the unique dispersion properties of light in the periodic structure of PhCs away from the photonic bandgap or sans the inclusion of defects. These dispersion properties of PhCs include: negative refraction, slow light effects, superprism effect and self-collimation. The ability to engineer the dispersion properties of PhCs allow researchers the possibility of controlling the propagation of light in ways that were not offered by PBG materials.

1.3 Theoretical Background

The coherent interactions of electromagnetic waves with the periodic structure of a PhC make the dispersion of light within it more complex than in materials found in nature [3]. Still, the propagation of electromagnetic waves in a PhC can be explained by Maxwell's equations using periodic boundary conditions dependent on the PhC structure. The source-free Maxwell's equations for a non-

magnetic and periodic linear dielectric structure, where $\mu(\mathbf{r}) = \mu_0$ and $\varepsilon(\mathbf{r}) = \varepsilon(\mathbf{r} + \mathbf{R}_n)^*$ can be written as,

$$\nabla \times \frac{1}{\varepsilon(\mathbf{r})} \nabla \times \mathbf{H} = -\frac{1}{c^2} \frac{\partial}{\partial t} \mathbf{H}, \text{ where } \nabla \cdot \mathbf{H} = 0 \quad (1.1)$$

$$\frac{1}{\varepsilon(\mathbf{r})} \nabla \times \nabla \times \mathbf{E} = \left(\frac{\omega}{c}\right)^2 \mathbf{E}, \text{ where } \nabla \cdot [\varepsilon(\mathbf{r})\mathbf{E}] = 0. \quad (1.2)$$

Since PhCs are periodic structures, we can use the Bloch theorem to simplify the multiple-lattice electromagnetic problem to a single cell unit [2], such that for a radial frequency ω and a Bloch wavevector \mathbf{k} ,

$$\mathbf{H}(\mathbf{r}, t) = e^{j(-\mathbf{k}\cdot\mathbf{r} + \omega t)} \mathbf{H}_{\mathbf{k}}(\mathbf{r}) \quad (1.3)$$

$$\mathbf{H}(\mathbf{r} + \mathbf{R}_n) = \mathbf{H}_{\mathbf{k}}(\mathbf{r}), \quad (1.4)$$

where $\mathbf{H}_{\mathbf{k}}$ is a periodic field. By substituting (1.3) in equation (1.1), it becomes a linear eigenvalue problem in the unit cell,

$$\hat{\Theta}_{\mathbf{k}} \mathbf{H}_{\mathbf{k}} = \left(\frac{\omega}{c}\right)^2 \mathbf{H}_{\mathbf{k}}, \quad (1.5)$$

where $\hat{\Theta}_{\mathbf{k}}$ is identified as the differential Maxwell operator with properties similar to the Hamiltonian operator in quantum mechanics,

$$\hat{\Theta}_{\mathbf{k}} \mathbf{H}_{\mathbf{k}} = [\nabla \times \frac{1}{\varepsilon(\mathbf{r})} \nabla \times] \mathbf{H}_{\mathbf{k}}. \quad (1.6)$$

From equations (1.5) and (1.6), we can observe that Maxwell's equations for photonic crystals are analogous to Schrodinger's equation, $\left[-\frac{\hbar}{2m} \nabla^2 + V(\mathbf{r})\psi = E\psi\right]$, with the boundary condition $V(\mathbf{r}) = V(\mathbf{r} + \mathbf{R}_n)$, which governs the behavior of electrons in semiconductor crystals. In semiconductor crystals, due to the coherent

superposition of partial scattering of the wave at each lattice, there are particular bands where propagation is prohibited, called bandgaps [3]. Similarly, when an appropriate structure is chosen for photonic crystals, a photonic bandgap will appear between two neighboring bands. When equation (1.5) is solved for the eigenfunctions of $\mathbf{H}_{\mathbf{k}}$, we obtain the dispersion relation of the medium, $\omega(\mathbf{k})$. Note that in a homogeneous material the dispersion relation,

$$k = \frac{\omega}{c} n, \quad (1.7)$$

where c is the speed of light in free space. Note that k depends on the refractive index, n , that is in turn related to the constitutive parameters of permittivity (ϵ) and the permeability (μ) of the material that describe its response to electromagnetic waves

$$n = \sqrt{\epsilon\mu}. \quad (1.8)$$

Also note that the group velocity, i.e., the velocity at which the envelope function of a wave packet propagates through space, is defined as

$$v_g(k_0) = \frac{d\omega}{dk}. \quad (1.9)$$

Therefore, it can be shown that for waves propagating in a photonic crystal the group velocity is equal to the k -gradient of the of the frequency ω ,

$$v_g(k_0) = \nabla_k \omega(k). \quad (1.10)$$

This dispersion relation of the dependence of the frequency on the wave vector can be depicted graphically using a dispersion diagram as the one shown in Fig. 1.1. The dispersion diagram plots the bands for \mathbf{k} -points that trace the perimeter of the

irreducible Brillouin zone. The vertical axis of the diagram shows the normalized frequency and the horizontal axis traverses k -space in multiple dimensions. In this dispersion diagram there is a bandgap (shown as a yellow stripe) above the top point of the first band and below the bottom point of the second band, located approximately between 0.3 -0.4 in the normalized frequency scale and there is another bandgap between the fourth and fifth bands.

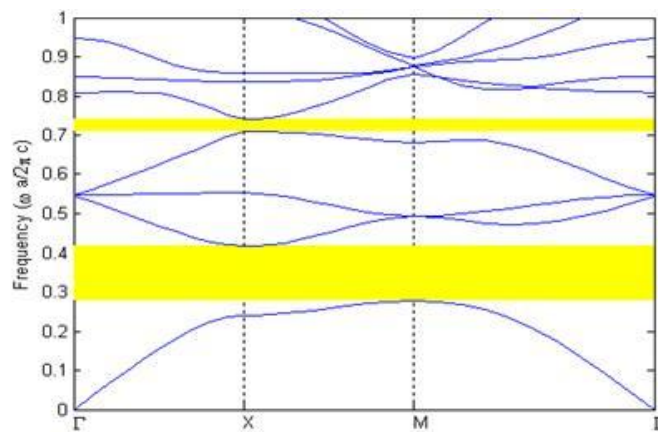


Figure 1.1 Dispersion diagram for a PhC with a photonic bandgap.

The dispersion surface is another graphical tool based on the dispersion relation, $\omega(\mathbf{k})$ that can be used to understand and engineer the dispersion properties of PhCs. These dispersion surfaces are also known as equifrequency surfaces (EFS) due to the fact that the dispersion relation refers to dispersion in frequency. An EFS represents a unique solution to Maxwell's equation in an irreducible Brillouin zone, where each horizontal slice of a dispersion surface represents an equifrequency contour (EFC), i.e., all k -vectors that can exist at that frequency; and each interception

between a dispersion surface and a constant-k line represents a single mode at different frequencies that can exist within the PhC lattice [3]. As an example, Fig. 1.2 shows the dispersion surface for a square-lattice PhC (this structure will be discussed more carefully in the following chapters of this thesis). Also, at the bottom of this figure we can see a projection of a horizontal slice of the dispersion surface, an EFC, which provides a valuable representation of the dispersion of light in the material, homogeneous or PhC, at that frequency.

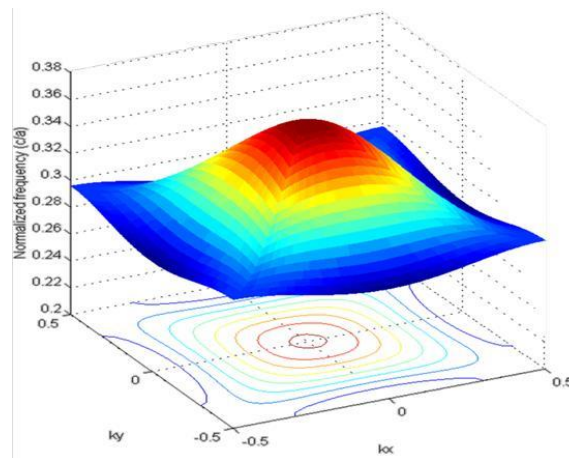


Figure 1.2 Dispersion surface and equifrequency contours for a square-lattice PhC.

Due to the complexity of the patterns in most PhC structures, it is not possible to resort to an analytical treatment as the one presented in this section; thus, the application of numerical methods is necessary to understand the interaction of light with the PhC structure. Given the popularity gained by PhC structures in the last two decades, significant efforts have been made to develop numerical algorithms to

analyze these periodic structures. The most popular of these numerical methods are the plane wave expansion method (PWEM), finite difference time domain method (FDTD), and the finite element method (FEM). A detailed description of these numerical techniques falls beyond the scope of this thesis, but the interested reader may consult Refs. 2 and 3 for further details. With these numerical methods and graphical tools such as the dispersion diagrams, dispersion surfaces and equifrequency contours, we have sufficient resources to understand and engineer the dispersion properties of PhCs. Our research and this thesis specifically are concerned with a singular dispersion property of PhCs, namely self-collimation.

1.4 Research Motivation and Thesis Outline

Recently substantial interest has arisen in the unique dispersion properties of photonic crystals; our research is particularly interested in the self-collimation property of 2D PhCs. Electromagnetic beams diverge when propagating in dielectric materials due to diffraction; however, the phenomenon of self-collimation in PhCs causes an electromagnetic beam to propagate within it without divergence, as if there were no diffraction in the material. The concept of self-collimation was originally introduced by Kosaka, *et al.* Their work was followed by Witzens, *et al.*, Chigrin, *et al.*, Yu, *et al.* [7, 8], and Chen, *et al.*, [9]. They further developed the concept and numerically simulated the propagation of electromagnetic waves with bending, crossing, and splitting in high-index-contrast (HIC) self-collimating (SC) PhCs. Lu *et al.* [7], extended the concept of self-collimation to low-index-contrast (LIC) PhCs and demonstrated numerically and experimentally the self-collimation of light in the

millimeter wave (mmW) regime. Starting from the later work on LIC PhCs, our research intended to address the issues that were not presented in their work: (1) Their 2D LIC PhCs were made of low-index dielectric slabs with a periodic array of cylindrical air holes, with our work we intend to demonstrate self-collimation for a PhC composed of a periodic pattern of dielectric rods held in place with a very low-index planar slab. (2) The actual transmission efficiencies of the PhCs were not measured directly or reported in their work. (3) The coupling structure presented in their work is only applicable to their design and the actual coupling efficiency was not reported. Another motivation for our research work on the periodic-rod-pattern PhC is that this structure is light in weight, electromagnetically invisible and mechanically strong, which makes it feasible for commercial applications in telecommunications. Furthermore, the purpose of our research is to design a SPhC structure with a transmission efficiency comparable to the established waveguiding technologies while providing the aforementioned advantages of a PhC “waveguide”. With this purpose in mind, we designed, fabricated and experimentally characterized the SPhC structures that are presented in the following chapters of this thesis.

In **Chapter 2**, we analyze the existing photonic crystal technologies organized into two broad categories: Photonic bandgap structures and dispersion-engineered PhC structures. For the photonic bandgap structures, we revisit the devices based on the incorporation of defects to PBG structures and provide a brief description of their applications. Then, we present the unique dispersion properties of PhCs, providing a brief description of each phenomenon, emphasizing on self-collimation.

In **Chapter 3**, we propose a two-dimensional, low-index-contrast PhC to demonstrate self-collimation of light in the microwave frequency regime. We

designed, and fabricated a PhC using a periodic array of low-index dielectric rods and experimentally demonstrated self-collimation, both in amplitude and phase, and measured the transmission efficiency for an LIC PhC slab. Upon the completion of our research with LIC SPhCs, we determined that it would be meaningful to extend our work to a High-Index-Contrast (HIC) PhC design to improve the confinement of light within the PhC. To validate this notion, in **Chapter 4**, we describe the design, numerical simulation, and fabrication of a PhC made with high-index ceramic rods. We also experimentally demonstrated a significant improvement in self-collimation compared to the LIC PhC.

In particular, we addressed the issue of coupling the PhC to a coaxial medium by designing an input/output (I/O) coupler. In **Chapter 5**, we describe the design and fabrication of this coupler and present the experimental results for coupling with both the HIC and LIC PhCs. In **Chapter 6**, we conclude this thesis and discuss the projected future direction of this effort in particular and this field of research in general.

Chapter 2

ANALYSIS OF PHOTONIC CRYSTAL STRUCTURES

2.1 Introduction

The behavior of electrons in semiconductor materials is governed by Schrodinger's equation, which contains fundamental physical constants like Planck's constant and the electron mass [3]. Therefore, directly scaling the dimensions of an electronic structure does not ensure that the properties of said device will remain unchanged at the different frequency of operation, in fact it can severely change the expected results. On the other hand, the behavior of electromagnetic waves in photonic crystals (PhCs) is governed by Maxwell's equations, which are scale-invariant with regard to the frequency of operation, except for possible variations in the permittivity and permeability [2]. As a result, the same PhC design can be scaled up to millimeter dimensions for microwave or millimeter-wave applications or scaled down to nanometer dimensions for near infrared (NIR) or visible light applications. Given the possibility of dimensional scaling in PhC designs, a device can be designed and fabricated in millimeter dimensions to verify the desired properties since the fabrication is less challenging than in nanometer scale, and find corresponding applications in other frequency regimes. Moreover, PhCs are considered the fundamental building block for large scale photonic integration. Justifiably, the

amount of research on PhCs has grown at an exponential rate in the last two decades, resulting in the discovery of a large variety of applications spanning from the RF to the NIR frequency regimes. In this chapter, we analyze and discuss some of the main applications of photonic bandgap structures and dispersion-engineered PhC structures, placing a particular emphasis on self-collimation.

2.2 Photonic Bandgap Structures

The current interest in PhCs can be traced back to the discovery of a photonic bandgap (PBG) in regions in the electromagnetic spectrum for certain periodic structures made with high-index dielectric materials. Due to the popularity of the early work, photonic bandgap (PBG) materials became synonymous with photonic crystals. In particular, two-dimensional PBG materials that can be realized with a periodic array of dielectric rods or a periodic array of air holes on a dielectric slab became the focus of this research due to the simplicity of their fabrication and analysis. The objective of the research was to implement these PBG structures for communications applications at subwavelength scales. Although several applications exist for PBGs alone, it was found that their optical properties can be altered by introducing defects in the periodic structure. Conceptually, the introduction of such defects is equivalent to doping in semiconductor materials, which is a fundamental part of the design of most semiconductor devices. In the following two sections we briefly discuss the properties and applications of point defects and line defects in photonics crystals, respectively.

2.2.1 Point Defect Implementation

A point defect can be introduced to a PhC by modifying a single lattice site of the periodic structure. By disturbing the symmetry of the PhC, defects allow for the localization of optical modes within that lattice site. Thus, strong confinement (or trapping) of photons can occur in structures with single defects [10], which leads to their application as microcavities. The characteristics of such microcavities can be tuned by modifying the shape or size of the defect. For instance, if a point defect spans a single lattice site (a hole or rod) in a PhC, then the cavity will support a single mode, but if the diameter of the defect is expanded it may confine multiple modes. The photon-trapping efficiency of a cavity is measured in terms of the quality factor Q , which for this purpose can be defined as [3]:

$$Q = \frac{f_{center}}{\Delta f}, \quad (2.1)$$

which implies that a narrow spectral width of the defect modes results in a high Q . It has been shown that a high Q for the microcavity can be attained by increasing the number of lattice layers and by reducing out-of-plane scattering in the PhC. Furthermore, an all-optical channel drop filter, capable of selectively dropping (or adding) photons from (or to) an optical network, can be designed by incorporating multiple cavities tuned for different frequencies on a single PBG material.

2.2.2 Line Defect Implementation

The propagation of photons within a PBG material can be controlled by introducing a coupled array of point defects. This array of point defects is known as a

line defect, and by incorporating it in a PBG material, the device can act as a dielectric waveguide that propagates light within confined path with low propagation loss. In Fig. 2.1(a) we provide a graphical rendition of a single line defect embedded in a photonic crystal. Figure 2.1(b) shows an FDTD simulation of the electric field distribution through a single line defect for a PBG with $r = 0.2a$. The dispersion diagram for a high-index-contrast (higher than 2) PBG material is presented in Fig. 2.2 (b). The group velocity approaches zero near the top of the first band shown in this dispersion diagram; guiding in this range in the bandgap with a line defect will significantly slow down light propagation.

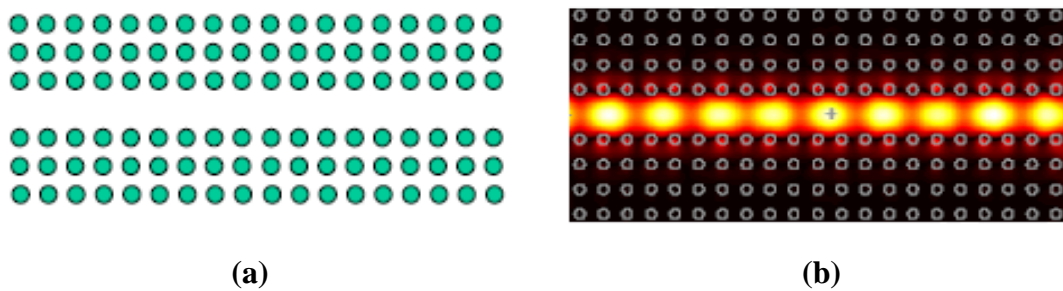


Figure 2.1. PBG material with implanted line defect, (a) graphical illustration of the structure, and (b) FDTD simulation of guided waves within the defect line.

Line defect waveguides in PhCs have received considerable attention because their waveguiding mechanism is fundamentally different from that of conventional dielectric waveguides that depend on total internal reflection, such as optical fibers. This fundamental difference provides properties that are not available with conventional waveguides. For instance, sharp bends can be realized with minimal or no bending loss [11]. Other notable applications for the strong confinement of light in these waveguides include zero crosstalk crossings and narrow band beam splitters.

2.3 Dispersion Engineered Photonic Crystal Structures

Most of the early interest in photonic crystals was centered on PBG materials, which with the insertion of defects have been shown to efficiently confine and propagate light [10, 11] within them. Yet, there are some issues that may limit their applications. For instance, these bandgap PhCs require a high index material, which makes it hard to couple them to standard electronic materials [7]. Also, these defect-based PhCs are rather inflexible since they can only control the propagation of light along the defect line and the fabrication tolerance is very low. In contrast, little interest was shown for applications based on the dispersion of waves outside the bandgap. This was mostly because outside the bandgap, the complex interactions of light with the structure of the PhC were very difficult to analyze [12]. This all changed with the illustration of the dispersion properties of PhCs through three-dimensional dispersion surfaces and equifrequency contours (EFCs). These tools gave researchers the ability to engineer the dispersion properties of photonic crystals providing a new paradigm for applications of PhCs. Dispersion-engineered PhCs facilitated the design of configurable devices, i.e., alterable media as the insertion of defects is not required. Because no bandgap is necessary, there is more material choice; we may choose low-index or high-index materials. There is also less constraint for tight fabrication tolerances.

Dispersion surfaces provide a graphical representation in k -space of the spectral properties of a certain band supported by the photonic crystal structure, i.e., they represent unique solutions to Maxwell's equation in an irreducible Brillouin zone. These dispersion surfaces are also known as equifrequency surfaces (EFS) due to the fact that the dispersion relation refers to dispersion in frequency. A horizontal slice of

a dispersion surface taken at a constant frequency is called an equifrequency contour (EFC), which represent all k -vectors that can exist at that frequency. The significance of the EFC profile is related to the dispersion relation

$$v_g(k_0) = \nabla_k \omega(k) \quad (2.1)$$

which states that light propagates in the direction of the gradient of the dispersion surface and perpendicularly to the EFC. Thus, the EFC helps us comprehend the spatial response of the modes excited within the photonic crystal structure and aids to determine the optical properties of the PhC. Accordingly, different PhC structures give rise to different EFCs which in turn produce different dispersion properties. For illustration purposes, in Fig. 2.2 we show dispersion surfaces for homogeneous media and for three different PhC structures.

The first band in the dispersion surface in Fig. 2.2 (a) shows the dispersion for an ordinary homogeneous material. The EFC for this band is a circle, and the phase velocity points in the same direction as group velocity, as a result the propagation of light in this material is isotropic. Figure 2.2(b) shows the dispersion diagram for a high-index-contrast, square-lattice PhC structure. This structure possesses the property of a photonic bandgap located above the top point of the first band where light propagation is forbidden unless defects are introduced. Near the top of the first band shown in Fig. 2.2(b), the group velocity approaches to zero close to the M-point. It will be shown in chapter 5 of this thesis, that guiding in this range without defects will remarkably slow down light propagation.

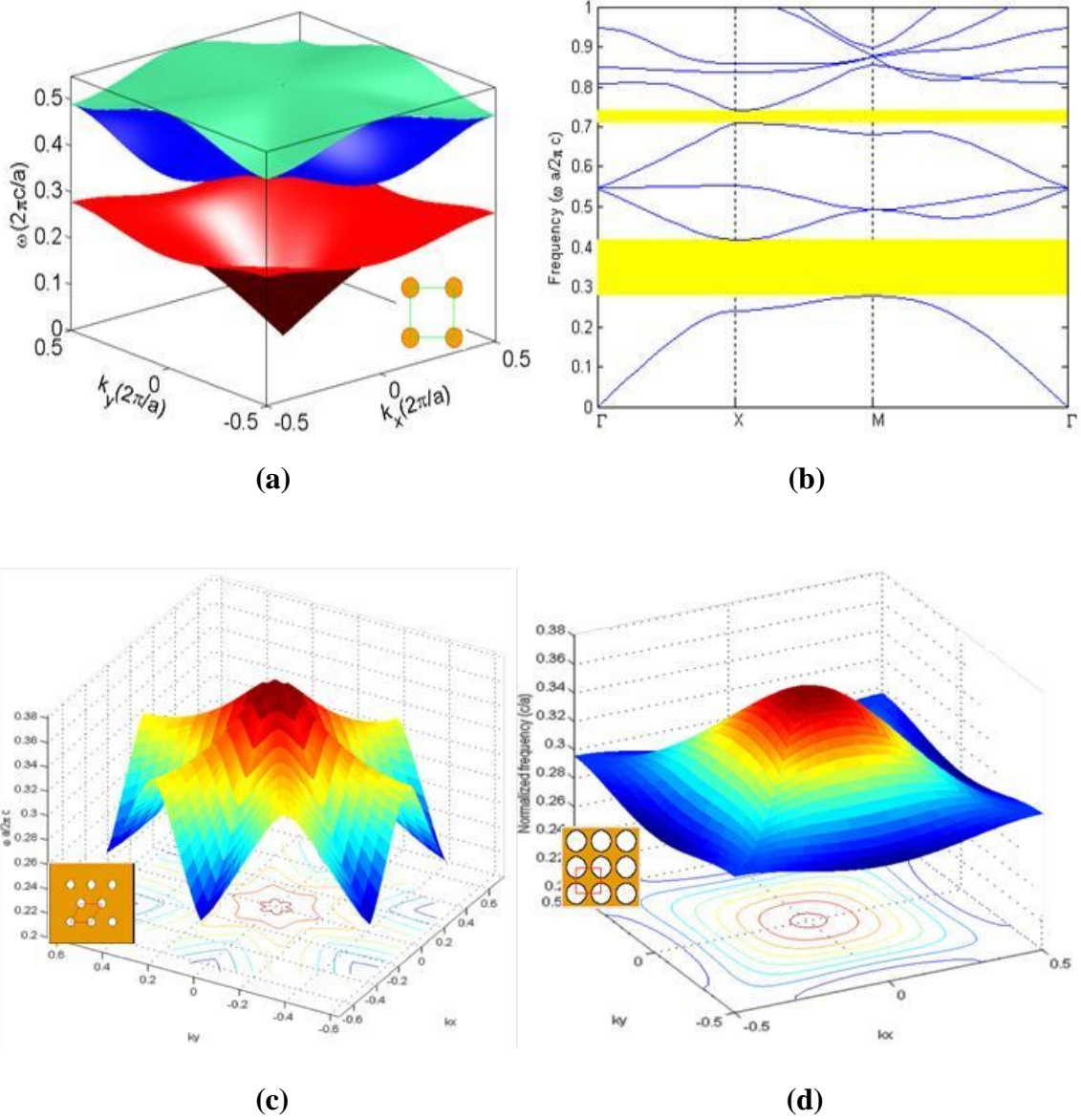


Figure 2.2 (a) Dispersion surfaces for a natural homogeneous material, (b) 2D dispersion diagram for a PBG material, (c) dispersion surface for a triangular-lattice PhC, and (d) dispersion surface for a square lattice PhC.

Another significant dispersion property of PhCs is the superprism effect. Figure 2.2(c) shows the third band dispersion surface for triangular-lattice PhC structure. This dispersion surface displays sharp corners, where group velocity changes abruptly with respect to the wavevector. In this case, a slight change in an incidence angle or the wavelength of the excitation will result in large change in the direction of propagation in the PhC. This dispersion is even more evident from the EFCs projected at the bottom of Fig. 2.2(c). This behavior justifies the denomination of superprism effect. The superprism PhC can be realized with the 3D FCC woodpile structure. Applications for the high sensitivity on the incidence angle or the wavelength of the excitation of the propagation direction that is offered by the superprism include passive wavelength demultiplexing and beam steering [3].

The dispersion surface shown in Fig.2.2 (d) corresponds to the second band in a square-lattice PhC structure. It can be seen that the slope of the dispersion surface is negative with respect to the k -vector; in this case, the phase velocity is opposite to the group velocity and the propagation of light, which gives rise to negative refraction. This means that when light is incident from a regular material into such a PhC, negative refraction occurs at the boundary. A negative refraction PhC is usually realized as a planar 2D square-lattice structure, but it can also take the shape of a 3D structure with a body-centered-cubic (BCC) lattice made of high-index dielectrics. Naturally, negative refraction in PhCs has found a niche in applications related with subwavelength imaging [8]. Additionally, applications have been found in electromagnetic trapping of neutral particles, that is, as electromagnetic “tweezers” [13].

At the edge of the band shown in Fig. 2.2(d) we can see that this dispersion surface possesses a flat profile. This is more evident with the nearly square contours in the EFCs projected at the bottom of this figure. These EFCs correspond to a group velocity that does not vary in direction of propagation with wavevector. The effect of this EFC is that in-plane light emitted incident to the flat contours will propagate within the PhC without diverging; this behavior is suitably known as self-collimation. To elucidate the self-collimation effect, in Fig. 2.3 we show a FDTD simulation of a point source located inside two structures with different dispersion properties: a homogeneous silicon slab, and one perforated with a square lattice of air holes, with $r/a = 0.3$. The EFC for the homogeneous material is circular, and therefore light waves emanate from the source isotropically and propagate in the same manner in the plane as shown in Fig. 2.3(a). In contrast, a square-lattice PhC has a nearly square EFC, thus for an isotropic source located at the middle of the PhC lattice the propagation is limited to narrow beams in the x- and y-directions, as in Fig. 2.3(b).

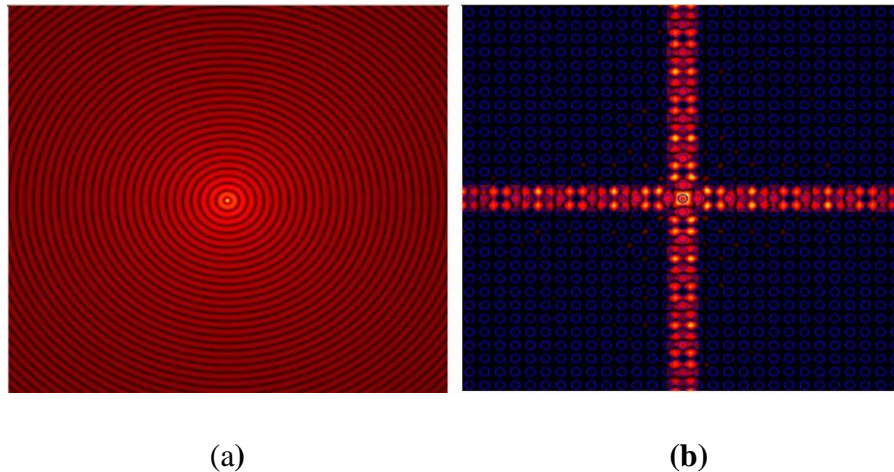


Figure 2.3 FDTD simulation of an electromagnetic light wave emanating from a point source when placed in a (a) homogeneous (unpatterned) silicon slab and (b) a silicon slab perforated with a square lattice of air holes.

In our research, we exploit the self-collimation phenomenon as it provides an alternative PhC structure that does not require defects for confinement of light and can still guide a beam of light in a particular direction without divergence. The dimension of the PhC components also permits the realization of structures on a scale comparable to the operation wavelength. Furthermore, in our self-collimating (SC) PhC design we use the first band dispersion surface, since the EFCs for this band lie outside the light cone, providing lower out-of-plane scattering and thus exhibiting better signal isolation. These SC PhCs have generally been realized as 2D square-lattice periodic structures, yet they have also been shown in slabs and 3D geometries. Due to this self-collimation effect, these photonic crystals have been used for applications in waveguiding and signal correlation.

Chapter 3

SELF-COLLIMATION OF LIGHT IN 2D LOW INDEX CONTRAST (LIC) PHOTONIC CRYSTALS

For most waveguiding applications, electromagnetic energy is emitted in beams of limited width, which implies the presence of a \mathbf{k} -vector perpendicular to the propagation direction. As a result, a beam of electromagnetic energy must diverge as it travels through space in a linear, homogeneous, isotropic material [2]. Rectangular metallic waveguides have generally been used to contain the diverging beams of light in homogeneous media. A motivation of our research is to design an alternative to conventional metallic waveguides that is composed of dielectric elements. As a solution, we designed a low-index-contrast (LIC) self-collimating photonic crystal (SCPhC) that reduces the diverging behavior of electromagnetic waves and propagates them in an arbitrary direction. This singularity is a consequence of the flat dispersion surfaces of some photonic crystals. We verified this behavior numerically with an HFSS simulation of electromagnetic waves propagating in a photonic crystal. We then fabricated the photonic crystals employing a low dielectric material and performed experimental acquisition of the field distribution in the PhC and measured the transmission efficiency of the PhC to demonstrate self-collimation in both amplitude and phase. In this chapter, we present the theoretical and experimental results for self-collimated transmission of electromagnetic waves in a two-dimensional LIC PhC in the microwave regime. As self-collimation is confirmed for this PhC structure we

present a novel guiding approach that also provides improved out-of-plane confinement, thus potentially eliminating crosstalk between optical channels.

3.1 Design of 2D LIC SPhC

This SPhC is realized by designing a lattice with a narrow range of group velocity directions [8]. If one were to design a material with a square EFC, then the group velocities would have the same direction, perpendicular to a straight side of the square EFC. Although a perfectly square EFC is elusive, to say the least, a square-like contour is achievable with a square-lattice PhC structure similar to the one shown in Fig 3.1. A basic design parameter for a 2D PhC is the lattice constant, a , which is very similar to the periodicity of a semiconductor crystal in nature [2], as seen in Fig. 3.1. The value of the lattice constant is generally expressed as a ratio to the wavelength of operation, and its ideal value can be determined from the dispersion contours of the photonic crystal shown in Fig. 3.2. The other important design parameters are the height of the slab, h , whose value is usually around $\lambda/2$; and the diameter of the rod (or hole in the opposite case), d , which is related to the diameter of the light cone and the lattice constant [12].

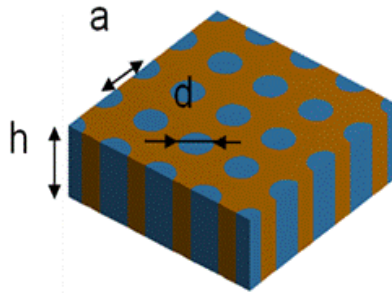


Figure 3.1 Illustration of a square-lattice PhC with its physical design parameters.

For our square-lattice PhC design, we used low index rods surrounded by a foam lattice that mimics the properties of free space. This design is best suited to guide TM polarized light, i.e., with the electric field parallel to the rods and the direction of propagation [2]. The low-index slab material is rigid Eccostock polyurethane foam, which was selected since its dielectric constant $\epsilon = 1.073 - j0.0023$, is very close to air. As the material for the rods, we chose Rexolite, which has a dielectric constant $\epsilon = 2.586 - j0.01484$, and a refractive index of 1.58. Rexolite is a polystyrene material that was selected due to its mechanical strength, low cost, low loss, ease of fabrication, and its low refractive index. This SCPhC is designed with low-index contrast between the slab and rods to reduce its electromagnetic signature and facilitate coupling with standard electronic materials. The index contrast between the Rexolite rods and the foam slab used in this SCPhC is only about 1.5.

It is also important to determine the effective index of the SCPhC slab, which is defined as

$$n_{eff} = n \sin \theta_{mode} \quad (3.1)$$

and can be found experimentally from the measured phase distribution along the PhC. It can also be calculated analytically as

$$n_{eff} = \frac{\lambda_0}{\lambda_g}, \quad (3.2)$$

where λ_0 is the wavelength of light in free space and λ_g is the wavelength of light guided along the PhC slab [7]. For this SCPhC we calculated, $n_{eff} = 1.23$. It is important to note that the dielectric constant varies slightly with frequency; hence, the values given for the dielectric constant of our materials were calculated at our

frequency of operation, which for this PhC is 12 GHz. At this frequency the wavelength of the light is $\lambda_0=25\text{mm}$. We used this information together with the plane wave expansion method (PWEM) to calculate and plot the EFCs for the square lattice PhC made of Rexolite rods on a polyurethane foam slab. These EFCs are as shown in Fig. 3.2. in terms of the normalized frequency

$$\omega_n = \frac{\omega a}{2\pi c} , \quad (3.3)$$

and the normalized wavevector

$$\mathbf{k}_n = \frac{\mathbf{k}a}{2\pi c} . \quad (3.4)$$

From these EFCs we anticipate that there will be self-collimation for $\omega_n = 0.45$ for transverse-magnetic (TM) modes. As seen in Fig. 3.2, at these frequencies the EFCs are nearly flat and the excited mode will propagate with group velocities pointing nearly in the same direction.

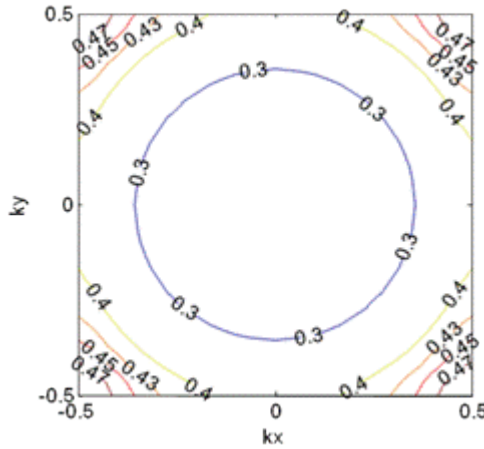


Figure 3.2 First band dispersion equifrequency contours for LIC SCPhC.

Under these conditions we chose the lattice constant $a = 0.45\lambda$ that corresponds to 11.25 mm. We also found the ideal height of our slab, $h = 1.2a$ corresponding to 13.5 mm, and the diameter of the Rexolite rods of $d = 0.9a$ corresponding to 9.53 mm. For $a = 0.45\lambda$, we can see the first band dispersion surface in Fig. 3.3(a), and the corresponding EFC in Fig. 3.3(b). The dispersion contour in Fig. 3.3(b) shows that only the light that is normal to the square side of the EFC will be guided in the direction of propagation at a given frequency. Since the first band at the selected frequency is 45° off-angle to the lattice orientation, for observational convenience we rotate the PhC lattice by 45° with respect to the feed for our simulations and experiments.

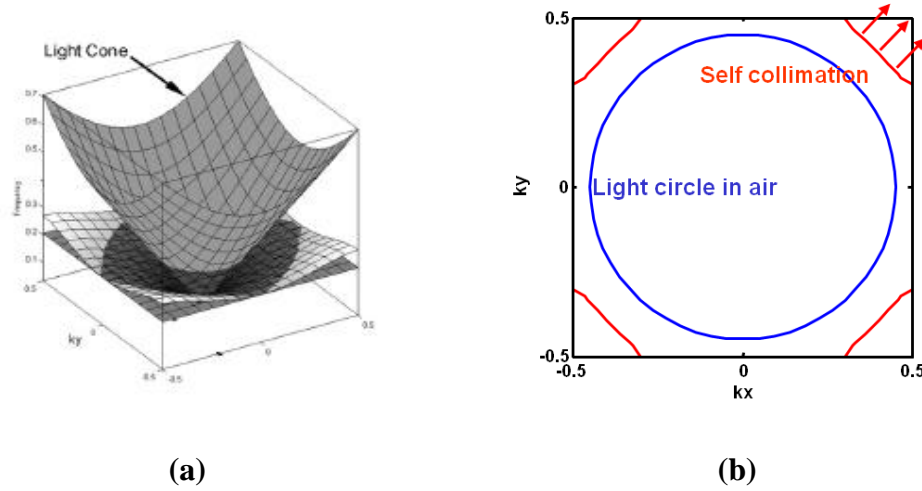


Figure 3.3 (a) First band dispersion surface of a PhC, and (b) equifrequency contours for our SPhC design for $a = 0.45\lambda$.

We chose the first band dispersion because the EFCs for these frequencies lie outside the light cone. The light cone represents the dispersion in the air, i.e., for $k_n = \omega_n$, where light cannot be fully confined in the vertical direction of the slab.

Consequently, this SCPhC design reduces the out-of-plane radiation compared to defect-based PBG materials because some modes may lie above the light cone for the PBG material, and some of the energy may be transferred to those modes [3]. In the case of the SCPhC, no modes lie above the light cone at their self-collimating frequency; therefore, nearly no energy is radiated out-of-plane. This principle is illustrated in Fig. 3.3(a), where the top surface represents the light cone and the surface under it is the first band dispersion surface of our SCPhC, which lies outside of the light cone.

3.2 Numerical Characterization of LIC SCPhC

Given the complexity of our SCPhC design, we resorted to numerical methods such as the Plane Wave Expansion Method (PWEM), the Finite-Difference Time-Domain Method (FDTD), and HFSS, which is a commercial full-wave Finite Element Method (FEM) simulation software, to design and simulate our SCPhC. We used PWEM to solve for the photonic band structure and dispersion surfaces of the LIC SCPhC [12, 14]. Following that, we used HFSS to integrate and simulate our designs. In this section we present an overview of the numerical simulations and results for the LIC SCPhC.

We used HFSS to simulate a microwave communications system including the Input/Output (I/O) couplers (this component of our design will be discussed in detail in Chapter 5 of this thesis) and a 24" LIC SCPhC. To feed this system we excited a plane wave at the back of the input coupler. This wave travels through the coupler, then propagates through the PhC and exits the system through the output coupler. We measure the electromagnetic waves that exit the system with a

plane wave detector at the end of the output coupler. In our early simulations, we connected the couplers to the PhC by placing their dielectric horn in contact with the first row of rods in the SCPhC, as shown in Fig. 3.4. From the electric field distribution also shown in Fig. 3.4 it is evident that there was still a significant impedance mismatch at the transition between the input coupler and the PhC, which is shown by the diverging light at the input of the PhC. This simulation resulted in an insertion loss of -3.6 dB at 12 GHz as shown in Fig. 3.10.

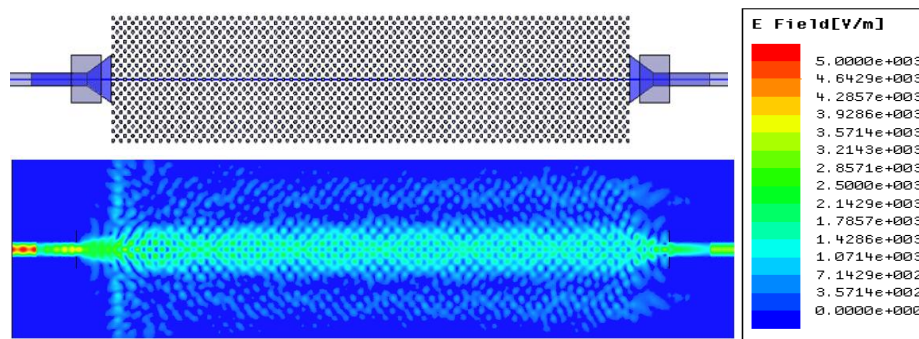


Figure 3.4 Simulated LIC SCPhC and its electric field distribution at 12 GHz.

To reduce the mismatch at the input of the PhC, we simulated a more gradual transition between the I/O couplers and the PhC [15]. We shifted the I/O couplers into the PhC slab and fused the dielectric transition of the coupler to the first row of rods in the PhC as shown in Fig. 3.5. For the electric field distribution shown in Fig. 3.5, the mismatch at the input coupler appears smaller than in Fig. 3.4, since the fields are not diverging as sharply at that transition. As expected, the numerical results from this simulation also improved, yielding an insertion loss of -2.8 dB for a 24-inch

PhC at 12 GHz. These numerical results are displayed with the experimental results in Fig. 3.10. Additionally, Fig. 3.6 shows the out-of-plane electric field distribution for the SCPPhC. As expected from the theory, this design exhibits efficient vertical confinement of the fields within the PhC.

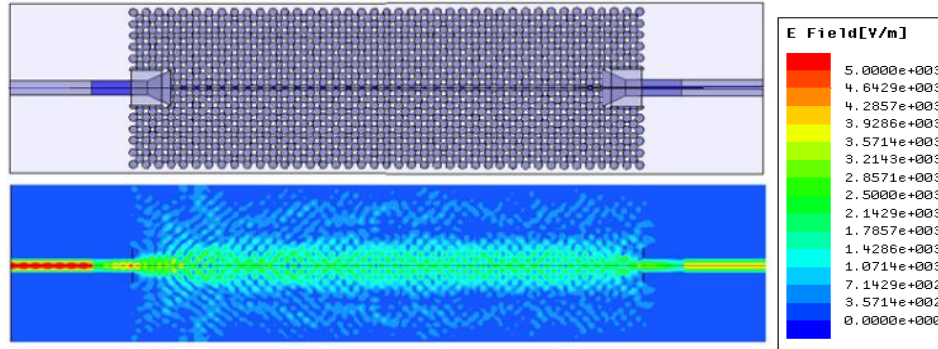


Figure 3.5 Simulated SCPPhC with shifted I/O couplers and its electric field distribution at 12 GHz.



Figure 3.6 Simulated electric field distribution for out-of-plane scattering for LIC SCPPhC.

3.3 Fabrication of LIC SCPPhC

Given the encouraging numerical results, we proceeded to fabricate the SCPPhCs in order to perform the experimental verification of our simulations. We fabricated the SCPPhC using a CNC router to drill the periodic lattice of cylindrical holes with diameter $d = 9.53$ mm and the lattice constant $a = 11.25$ mm on the

Eccostock polyurethane foam slab. The Rexolite rods were available from the supplier with the desired diameter of 9.53 mm, but the length of each rod was 6 ft. We used an automated lathe to cut nearly two thousand Rexolite rods to the desired height of 13.5 mm with a fabrication tolerance of $\pm 0.002''$. Subsequently, we used these rods to fill the periodically drilled holes in the polyurethane foam slab. A picture of the complete slab is shown in Fig. 3.7.

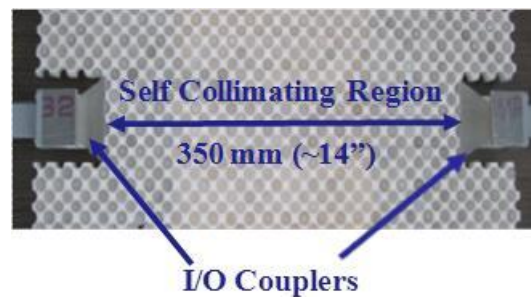


Figure 3.7 Fabricated SCPhC connected to I/O couplers for experimental measurement of transmission efficiency.

3.4 Experimental Demonstration of Self-Collimation in LIC PhC

To verify the self-collimating behavior of the PhC we setup a microwave imaging system composed of an Agilent 8722B network analyzer, a motion control system, and an S-parameter measurement system. In our setup, the sample is placed next to the detector with a dielectric I/O coupler as the input source as seen in Fig. 3.8. We chose a 1mm monopole antenna as the detector that captures signal and outputs it back into port 2 of the network analyzer. The field distribution is acquired by scanning the surface of the PhCs to detect the evanescent waves of the fields propagating in the slab. We leave a gap of approximately 5mm between the detector and the surface of

the PhC and we assume that the evanescent wave distribution is proportional to the field inside the PhCs. We fed this PhC with our hybrid I/O coupler that excites the TE_{01} mode and we positioned the coupler such that the E-vector was perpendicular to the PhC slab to coincide with the detecting monopole antenna whose tip is pointed straight at the slab. We set the frequency of the feed signal at 12 GHz and scanned the slab with step $dx=dy=1.5\text{mm}$. We developed a custom Labview program to synchronize the motion of the 2D scanning system and the measurement of the signals in the network analyzer. For each step in the scan, an S-parameter value is collected and depicted as a part of an image. Therefore, each pixel in the image corresponds to the S_{21} value at that position. In addition, in the VNA the S-parameter is given as complex values, so both amplitude and phase distributions can be obtained in one measurement.

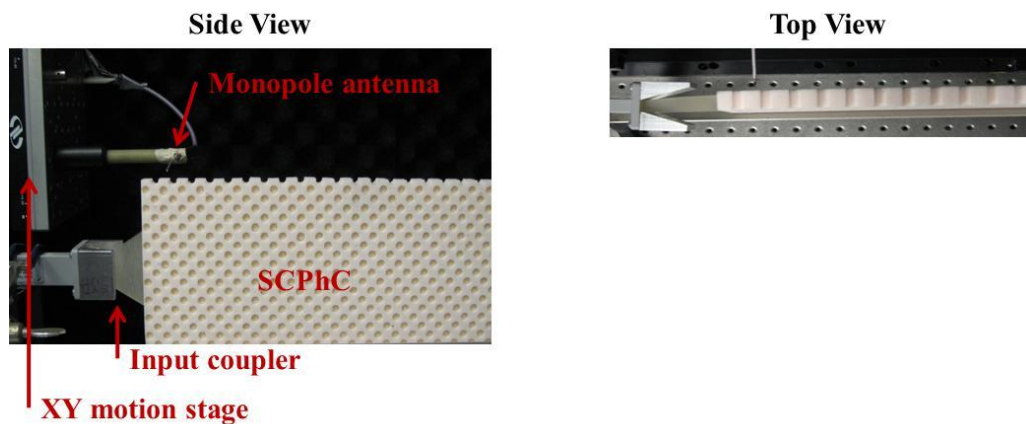


Figure 3.8 Experimental setup for 2D scanning of SCPhC.

Figure 3.9 (a, b) shows the experimental results for amplitude and phase of the electric field distribution. The distribution of E_z , both in amplitude and phase, shows that the propagation is only along one direction through the center line of the

picture and the microwave signal is indeed self-collimated through the PhC. The beat shown in the amplitude might be attributed to the activity of harmonic modes excited in the second or higher Brillouin zones.

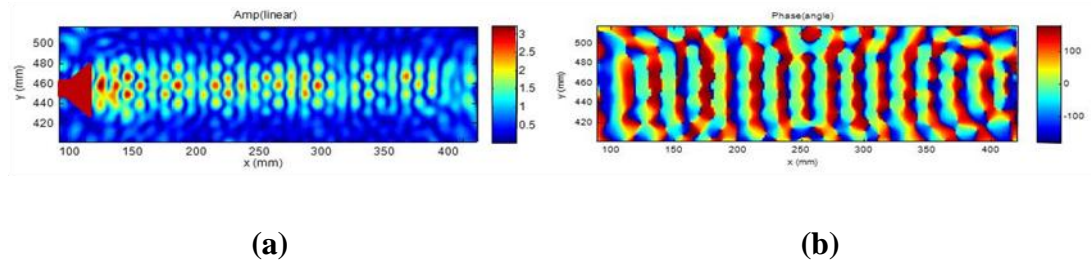


Figure 3.9 Measured electric field distribution for 12-inch LIC PhC (a) amplitude, and (b) phase.

3.5 Experimental Verification of Transmission Efficiency in LIC SCPhC

For the experimental verification of the numerical results we setup an microwave measurement system that included an Agilent 8722B network analyzer, two sets of 3.5 mm coaxial cables, the two I/O couplers and the LIC SCPhC. We then performed the necessary calibration of the network analyzer using “Open-Short-Load” standards and a TRL method to guarantee the accuracy of our measurements. For the experimental measurement of the insertion loss through the I/O couplers and the SCPhC, first we connected port 1 of the network analyzer using a 3.5 mm coaxial cable to the coaxial-waveguide transition of the input coupler of our system. This coupler fed a beam to the PhC through the dielectric transition that was fused to the first row of rods of the PhC. Similarly, the output coupler was connected at the other

end of the PhC to couple the beam propagated through the SCPhC to the second port of the network analyzer. This experimental setup is shown in Fig. 3.7.

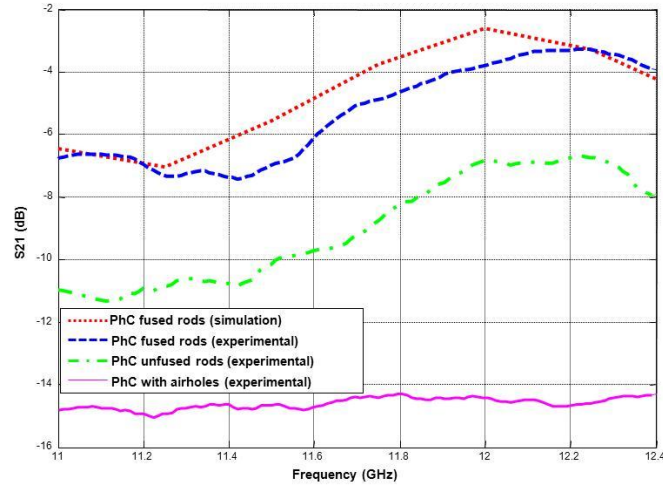


Figure 3.10 Numerical and experimental results for insertion loss for LIC SCPhC.

Using this setup, we measured the transmission through the SCPhC, yielding an insertion loss of -3.29 dB through the SCPhC slab at 12.1 GHz. These experimental results and the numerical results are presented graphically in Fig. 3.10. We can see also in Fig. 3.10 that there is a significant improvement, of about 4 dB, in the transmission through the I/O couplers and SCPhC when the dielectric transitions of the couplers are shifted into the PhC slab and fused to the first row of rods. The experimental results for the PhC with rods fused to the coupler show close agreement to the results of the numerical simulations, with only slight variations that could be attributed to the fabrication tolerance. Furthermore, we experimentally measured the transmission through a foam lattice with cylindrical air holes, demonstrating complete signal suppression and making it clear that the propagation in this slab is not

collimated. This measurement served to prove that the collimation in our PhC is not attributed to the horn but to the dispersion properties of the PhC.

We also set out to determine and isolate the coupling and transmission loss components of the insertion loss in our integrated SCPhC system. We define the coupling loss, L_c , as the component of the insertion loss caused by the transition, through the I/O couplers, from the coaxial medium to the SCPhC (this component will be discussed in depth in Chapter 5 of this thesis). In a similar manner, we define the transmission loss, L_t , as the component of the insertion loss that results from the in-plane divergence of waves in the SCPhC. In order to isolate the loss components, we fabricated two more LIC PhC slabs of 9.1" and 16.6" in length. Exploiting the flexibility and homogeneity of our SCPhC design, which allows us to feed a signal arbitrarily along the width or length of the slab, we were able to measure the insertion loss for five different lengths, 6.6", 9.1", 11.6", 14.1", 16.6", using only three different slabs. We experimentally measured the insertion loss for the five different PhCs, obtaining the results presented in Fig. 3.11. These measurements yielded a good agreement with the numerical results for the same PhC lengths.

Using the results shown in Fig. 3.11, we picked a data point at 12.1 GHz for each PhC length and plotted a single line for the insertion loss for PhC's of different lengths at 12.1 GHz. This result allowed us to compute the coupling loss component, making it trivial to determine the transmission loss component of the photonic crystal by simply subtracting the total coupling loss component from the insertion loss for the complete system. The resulting total transmission loss was calculated as -1.96 dB for the 11.6" PhC; accordingly, we calculated the transmission

loss component per unit length as $L_t = -0.17 \pm 0.01 \text{ dB}/\lambda$, $0.17 \pm 0.01 \text{ dB}/\text{inch}$ at 12.1 GHz.

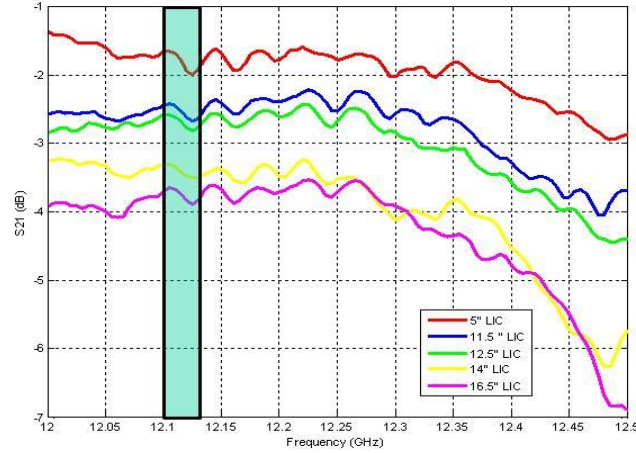


Figure 3.11 Measured transmission loss for different length slabs for LIC PhC.

3.6 Discussion and Conclusions

To summarize, in this chapter we have successfully demonstrated self-collimation in low-index-contrast PhCs in the microwave regime. We designed and fabricated LIC PhCs based on a pattern of Rexolite rods on an Eccostock foam lattice and experimentally demonstrated self-collimation, both in amplitude and phase, and measured the transmission efficiency for an LIC PhC. We demonstrated that this SCPhC provides signal isolation, with minimal out-of-plane scattering of light and that it can be used efficiently for waveguiding in practical applications. It has been shown that these dispersion-engineered PhCs offer superior configurability, have less stringent requirements in fabrication and permit a greater choice of materials than photonic bandgaps; hence, it is expected that they will assume an important role in the

large-scale integration of photonic devices. In the microwave regime, the further development of this guiding technology resulting in competitive transmission efficiencies would enable its applications for local large area communications systems. With this objective in mind, we used the knowledge acquired from the results for this LIC PhCs to extend our work to a high-index-contrast (HIC) PhC design that would improve the confinement of light within the PhC. We present this work in the next chapter of this thesis.

Chapter 4

HIGH INDEX CONTRAST (HIC) SELF-COLLIMATING PHOTONIC CRYSTAL

Although the propagation loss that we measured (Chapter 4) for the low-index-contrast (LIC) photonic crystal (PhC) was lower than what had been reported for equivalent self-collimating designs at this frequency, the transmission efficiency was not sufficiently high to compete with the established waveguiding mechanisms in the microwave regime. Theoretically, for high-index contrast (HIC) PhCs it is easier to achieve self-collimation since the energy is confined in-plane better within the higher-index material and the out-of-plane scattering is also lower for such a PhC. The results achieved for LIC PhCs presented in the previous chapter provided principal insights into self-collimation that allowed us to extend our work to a HIC PhC design in order to improve the confinement of light within the PhC.

4.1 Design of 2D HIC SCPPhC

For this PhC design, we used a square-lattice structure composed of high index rods surrounded by a foam lattice that mimics the properties of free space. This PhC is designed to guide TM polarized light, i.e., with the electric field parallel to the rods and the direction of propagation [2]. The low-index slab material is rigid Eccostock polyurethane foam, which was selected since the value of its dielectric

constant $\epsilon = 1.073 - j0.0023$, is very close to air. As the material for the rods, we chose ceramics (95% Al_2O_3) with a dielectric constant $\epsilon = 9.1$, and a refractive index of 3.1. The choice of ceramic rods is related to its physical properties which are similar to those of the polystyrene material that was used for the LIC PhC; hence, ceramics also offer mechanical strength, and low loss. Given the high refractive index of the ceramic rods we achieved an index contrast ratio of 3:1 between the rods and the foam slab. We used this information about the materials together with the plane wave expansion method (PWEM) to calculate and plot the EFCs for the square lattice PhC made of ceramic rods on a polyurethane foam slab. The resulting EFCs for the first band dispersion surface are as shown in Fig. 4.1 in terms of the normalized frequency and the normalized wavevector. We chose the first band dispersion because the EFCs for these frequencies lie outside the light cone; thus, the guided mode is ensured in the vertical direction.

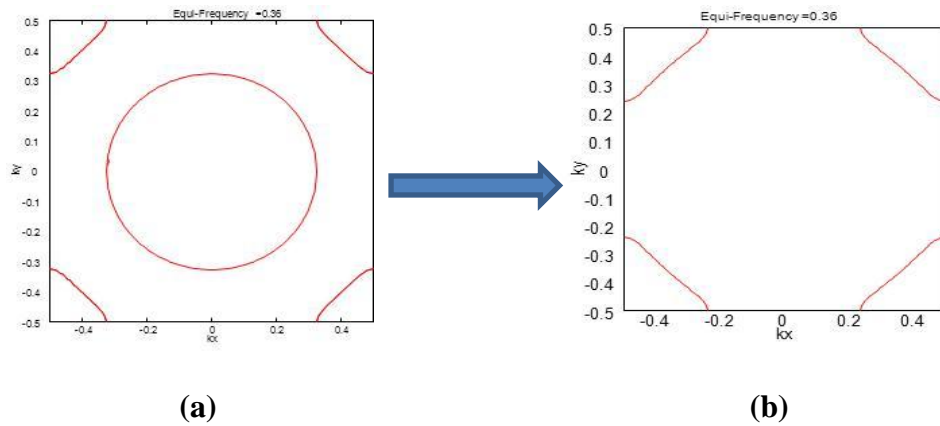


Figure 4.1 (a) 3D EFCs for $a = 0.36\lambda$ for HIC SCPhC, and (b) equivalent 2D EFCs for HIC PhC.

The design of this HIC PhC presented a particular challenge that we had not faced for the LIC PhC. Since this design uses high-index rods, the desired self-collimating behavior is achieved with smaller rods and lattices; thus, increasing the complexity of the problem for numerical simulations. The effect of this increase in complexity is that our 3D numerical simulators in HFSS and FDTD were unable to process the structure in acceptable time intervals. In order to reduce the complexity of the 3D simulation, a 2D dispersion surface was generated which matched closely to the 3D dispersion surface. This equivalent 2D dispersion diagram is obtained by optimizing the effective refractive index ($n = 1.9$) of the 2D PhC. The 3D PWEM simulation of the EFC for $a = 0.36\lambda$ is shown in Fig. 4.1(a). The matched 2D EFC is shown in Fig. 4.1(b).

We used these 2D EFCs iteratively with a 2D FDTD simulation of the HIC PhC to optimize the dimensions of the lattice. In this manner we were able to design a nearly square EFC for the first dispersion band of this PhC such that the group velocities having the same direction, perpendicular to a straight side of the square EFC would be incident upon a larger spatial angle for self-collimation. The EFC shown in Fig. 4.2 represents the dispersion for the HIC PhC for $a = 0.36\lambda$, and it shows that the spatial angle for self-collimation is 28 degrees, which represents an improvement of nearly 8 degrees compared to the LIC PhC. From these EFCs we anticipated that there would be self-collimation for $\omega_n = 0.36$, that is, for $a = 0.36\lambda$ for transverse-magnetic (TM) modes. For this SCPhC we calculated the effective index of the HIC PhC as $n_{eff} = 1.9$. It is important to note that the dielectric constant varies slightly with frequency; hence, the values given for the dielectric constant of our materials were calculated at our frequency of operation, which for this PhC is

10.1GHz. At this frequency the wavelength of the light is $\lambda_0=30\text{mm}$. The height of the rods has been optimized to obtain a flat dispersion surface for self-collimation. We found the ideal height of our slab, $h = a$ corresponding to 10.6 mm, and the diameter of the ceramic rods of $d = 0.6a$ corresponding to 6.35 mm. Since the first band at the selected frequency is 45° off-angle to the lattice orientation, for observational convenience we rotate the PhC lattice by 45° with respect to the feed for our simulations and experiments.

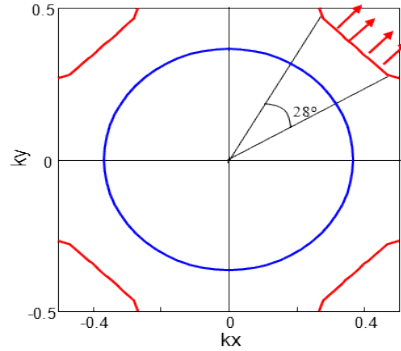


Figure 4.2 EFC of HIC SCPhC for $a = 0.36\lambda$, showing the spatial angle for self-collimation.

4.2 Numerical Characterization of HIC SCPhC

Given the complexity of our SCPhC design, we resorted to numerical methods such as the Plane Wave Expansion Method (PWEM) and the Finite-Difference Time-Domain Method (FDTD) to design and simulate our HIC PhC. We used PWEM to solve for the photonic band structure and dispersion surfaces of the HIC PhC. Following that, we used a 2D FDTD algorithm to integrate and simulate our

designs. In this section we present an overview of the numerical simulations and results for the HIC SCPhC.

Since this HIC PhC design was much more complex than the LIC design, we were not able to use our 3D HFSS and 3D FDTD simulation engines to numerically simulate a transmission through the PhC. Instead, we simulated the HIC PhC using a 2D FDTD algorithm by optimizing the effective index of the 2D PhC to match with a 3D simulation. To feed this system we excited a Gaussian beam at the back of the input coupler. This wave travels through the coupler, then propagates through the PhC and exits the system through the output coupler. We measure the electromagnetic waves that exit the system with a Gaussian beam detector at the back end of the output coupler. This simulation setup is shown in Fig. 4.3, and it includes the two I/O couplers and the HIC PhC.

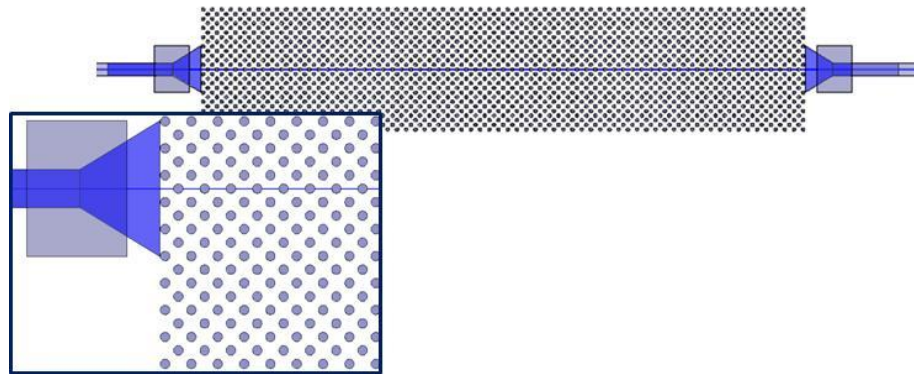


Figure 4.3 Simulation setup for HIC PhC, including the two I/O couplers and the 2D HIC PhC.

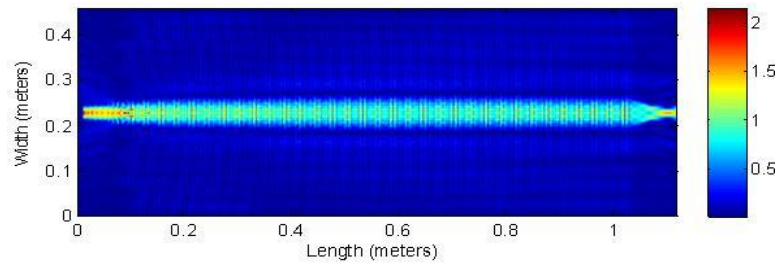


Figure 4.4 FDTD simulation of electric field distribution for HIC PhC at 10.1 GHz.

Based on the setup shown in Fig. 4.3, we simulated the field distribution for a 1-meter-long HIC PhC to gain qualitative knowledge of the propagation of the waves within the field. We used this simulation iteratively with the PWEM simulation of the band structure of the PhC to optimize its dimensions. The result of this optimization process is shown in Fig. 4.4, which displays the electric field distribution for the HIC PhC for $a = 0.36\lambda$ at a frequency of 10.1 GHz. This simulation was characterized quantitatively by estimating the fraction of the input power captured at the output detector. These numerical results are displayed in Fig.4.5, in terms of the insertion loss (dB) through the length of the PhC. The blue ripple pattern shown in Fig. 4.5 is plotted from the numerical data captured for the simulation and the red line is a linear approximation of the trend of the data. The insertion loss of the simulated HIC PhC was approximately 1 dB for a 1 meter transmission. The results displayed in Fig. 4.5 do not include the insertion loss due to the couplers. Additionally, since this simulation is two-dimensional, it does not contain any information about the height of the PhC so these results do not account for the out-of-plane scattering loss.

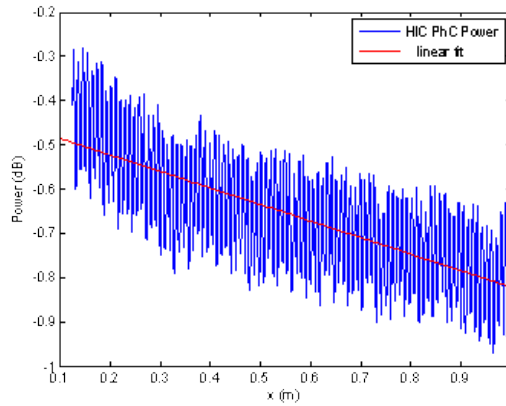


Figure 4.5 Numerical results for insertion loss for FDTD simulation of HIC PhC at 10.1 GHz.

4.3 Fabrication of HIC SCPhC

Given the encouraging numerical results, we fabricated the HIC PhCs in order to verify them with experimental measurements. We fabricated the PhC using a CNC router to drill the periodic lattice of cylindrical holes with a diameter $d = 6.35$ mm and the lattice constant $a = 10.6$ mm on the Eccostock polyurethane foam slab. We found the ideal height of the rods is $h = a$ corresponding to 10.6 mm. The design of the PhC was tuned to the appropriate frequency to accommodate the diameter of the ceramics rods that were available from the manufacturer. Since ceramics are higher-index materials, they are also denser and mechanically harder than the polystyrene material used for the LIC PhC. As a result, cutting and machining ceramics requires very advanced macro-machining tools, like grinders and water-jet cutters. Fortunately, for this design the ceramic rods were available from the manufacturer with the desired height of 10.6 mm. Subsequently, we used these rods to fill the periodically drilled

holes in the polyurethane foam slab. A picture of the fabrication components and the complete PhC is shown in Fig. 4.6.

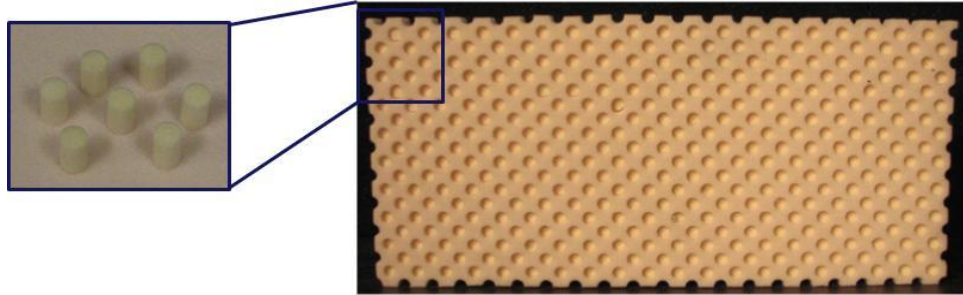


Figure 4.6 Fabrication components for HIC PhC.

4.4 Experimental Demonstration of Self-Collimation in HIC PhC

To verify the self-collimating behavior of the PhC we setup a microwave imaging system composed of an Agilent 8722B network analyzer, a motion control system, and an S-parameter measurement system. In our setup, the sample is placed next to the detector with a dielectric I/O coupler as the input source as seen in Fig. 3.8 in the previous chapter. We chose a 1mm monopole antenna as the detector that captures signal and outputs it back into port 2 of the network analyzer. The field distribution is acquired by scanning the surface of the PhCs to detect the evanescent waves of the fields propagating in the slab. We leave a gap of approximately 5mm between the detector and the surface of the PhC and we assume that the evanescent wave distribution is proportional to the field inside the PhCs. We fed this PhC with our hybrid I/O coupler that excites the TE_{01} mode and we positioned the coupler such

that the E-vector was perpendicular to the PhC slab to coincide with the detecting monopole antenna whose tip is pointed straight at the slab. We set the frequency of the feed signal at 10.1 GHz and scanned the slab with step $dx=dy=1.5\text{mm}$. We also developed a custom Labview program to synchronize the motion of the 2D scanning system and the measurement of the signals in the network analyzer.

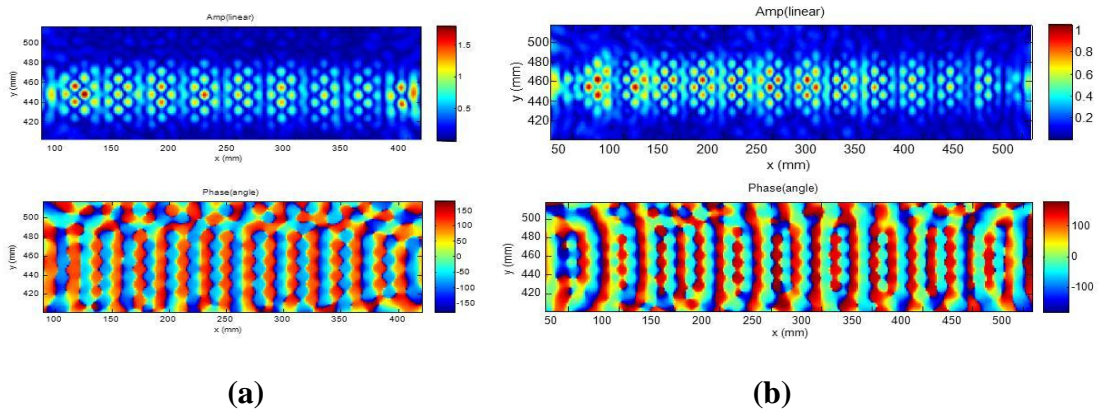


Figure 4.7 Measured electric field distribution amplitude and phase fronts for HIC PhC for (a) 12 inch slab, and (b) 18 inch slab.

Figure 4.7 (a, b) shows the experimental results for amplitude and phase of the electric field distribution of a 12-inch and a 18-inch PhC, respectively. The distribution of E_z , both in amplitude and phase, shows that the propagation is only along one direction through the center line of the picture and the microwave signal is indeed self-collimated through the PhC. The beat shown in the amplitude might be attributed to the activity of harmonic modes excited in the second or higher Brillouin zones.

4.5 Experimental Verification of Transmission Efficiency in HIC SCPhC

For the experimental verification of the numerical results we setup an microwave measurement system that included an Agilent 8722B network analyzer, two sets of 3.5 mm coaxial cables, the two I/O couplers and the LIC SCPhC. We then performed the necessary calibration of the network analyzer using “Open-Short-Load” standards and a TRL method to guarantee the accuracy of our measurements. For the experimental measurement of the insertion loss through the I/O couplers and the SCPhC, first we connected port 1 of the network analyzer using a 3.5 mm coaxial cable to the coaxial-waveguide transition of the input coupler of our system. This coupler fed a beam to the PhC through the dielectric transition that was fused to the first row of rods of the PhC. Similarly, the output coupler was connected at the other end of the PhC to couple the beam propagated through the SCPhC to the second port of the network analyzer.

Using this experimental setup, we measured the transmission through a 12” HIC at a frequency of 10.1 GHz, resulting in an insertion loss of -1.61 dB. This measurement shows that the transmission in HIC PhC was 0.84 dB higher compared to the LIC PhC measured under the same conditions. The insertion loss for an 11.5” LIC PhC measured at 12.1 GHz was -2.45 dB. These results are displayed graphically in Fig. 4.8, where the red line plots the HIC experimental data and the blue line plots the LIC experimental data. The PhCs were not compared at the same frequency because of fabrication constraints. Since the stated purpose of our research was to fabricate a SCPhC waveguide in the microwave regime, particularly in the X-band (8 – 12.4 GHz), the LIC PhC was designed to operate at 12 GHz based on the diameter of Rexolite rods that were available from the manufacturer, but for the dimensions of the

available ceramic rods that fit our HIC design, the closest frequency of operation was 10.1 GHz. Despite this slight variation, the frequencies are close enough that a direct comparison of the transmission through the two PhC structures is valid.

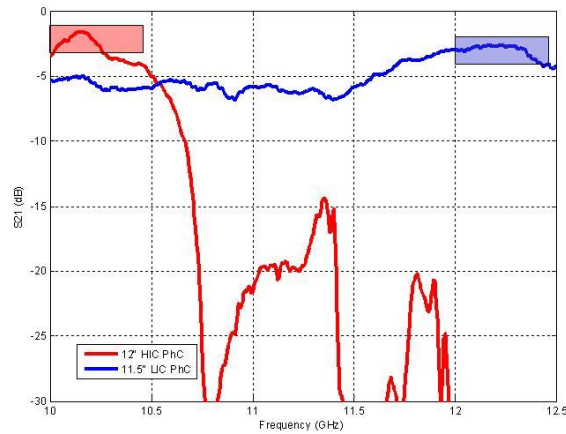


Figure 4.8 Transmission loss comparison between HIC and LIC PhC.

As we did for the LIC PhC, we set out to determine and isolate the transmission loss component of the insertion loss in our integrated SCPPhC system. We define the transmission loss, L_t , as the component of the insertion loss that results from the in- plane divergence of waves in the SCPPhC. In order to isolate the loss components, we also fabricated an 18-inch HIC PhC slab. Exploiting the flexibility and homogeneity of our SCPPhC design, which allows us to feed a signal arbitrarily along the width or length of the slab, we were able to measure the insertion loss for four different lengths, 6", 12", 18", and by putting the 12" and 18" together, 30". We experimentally measured the insertion loss for the four different PhCs, obtaining the results presented in Fig. 4.9.

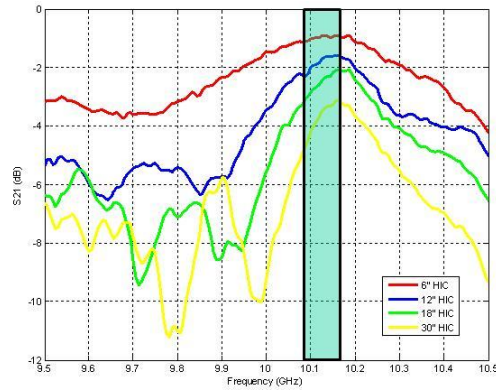


Figure 4.9 Measured transmission loss for different length slabs of HIC PhC.

Using the results shown in Fig. 4.9, we picked a data point at 10.1 GHz for each PhC length and plotted a single line for the insertion loss for PhCs of different lengths. This result allowed us to compute the coupling loss component, making it trivial to determine the transmission loss component of the photonic crystal by simply subtracting the total coupling loss component from the insertion loss for the complete system. The resulting total transmission losses that we calculated for both the LIC and HIC PhCs are displayed together in table 4.1 for comparison purposes. From this data we calculated the transmission loss component of the HIC PhC per unit length as $L_t = -0.09 \pm 0.005$ dB/ λ , which corresponds to $L_t = -0.08 \pm 0.005$ dB/inch, that is, $L_t = -3.14 \pm 0.2$ dB/m at 10.1 GHz. These results represent an improvement in transmission by a factor of 2 compared to the LIC PhC.

Table 4.1 Transmission loss data for HIC and LIC PhC slabs of different length.

LIC PhC Length (inches)	Transmission (dB) 12.1 GHz	HIC PhC Length (inches)	Transmission (dB) 10.1 GHz
5	-1.66	6	-0.93
12.5	-2.61	12	-1.61
14	-3.3	18	-2.2
16.5	-3.69	30	-3.2

Chapter 5

COAXIAL-TO-PHC COUPLING FOR INTEGRATION IN THE MICROWAVE REGIME

5.1 Introduction

The application of the aforementioned SPhCs requires their integration within a communications system in the microwave frequency regime. Since the most common and efficient method of outputting light at this frequency range is a coaxial SMA (subminiature A) connector, it was necessary to design a structure to couple, i.e., feed electromagnetic energy from this coaxial medium into the 2D PhC slab and back out to the coaxial medium. We researched different options to fulfill this requirement including coaxial-to-rectangular-waveguide transitions and dielectric slab waveguides, as well as microstrip-to-dielectric line transitions [16, 17]. These couplers individually did not yield the desired coupling efficiency due to a large mismatch at the transition with the PhC. The insertion loss for these transitions still exceeded 3 dB at our frequency of operation, yet we were able to utilize some of the same concepts from the microstrip-to-dielectric transition to design a new coupling structure.

5.2 Coupler Design

We designed a coaxial-to-PhC, Input/Output (I/O) coupler to reduce the insertion loss due to the transition from a coaxial medium to a 2D photonic crystal slab. This coupler is a hybrid design that combines commercially available parts

including a coaxial-to-rectangular waveguide transition and a WR 90 waveguide (which guides waves in the X-band frequency range, from 8 – 12.4 GHz), with original designs including a vertically-tapered dielectric line, a horizontally tapered dielectric horn and two vertically-tapered metallic flanges.

At the coaxial-to-waveguide adapter, the TEM mode of the coaxial medium is gradually matched to the dominant waveguide mode. Although the fundamental mode of the dielectric line is not TEM, its field configuration is very similar to a quasi-TEM mode [16, 17]; thus, the dielectric line facilitates mode matching. This dielectric line was designed with a width/height aspect ratio that decreases gradually with a 7 degree vertical taper, such that the height of the dielectric line is 1 cm at its largest point, same as a WR90 waveguide; and only about 1 mm at its smallest point. In reference 16, it is shown that such a tapered dielectric line improves the coupling to the TEM modes from the coaxial medium since the SWR measured at the transition is reduced by 50% compared to a rectangular dielectric line. We added to this dielectric line a horizontally-tapered dielectric horn. The dielectric horn has a horizontal angle of 40 degrees on each side. The purpose of the dielectric horn is to expand the width of the guided beam from 1cm to 3cm, thus limiting the \mathbf{k} -vector and reducing the divergence of the fields. Additionally, at this greater width the horn matches the impedance within the metallic waveguide to the impedance at the input of SCPhC. Finally, we added two tapered metallic flanges at the open end of the WR90 waveguide to contain any out-of-plane radiation from the dielectric horn.

5.3 Numerical Characterization of Coupler Performance

Based on the design principles discussed above, these I/O couplers were simulated numerically to optimize their dimensions prior to fabrication. For the numerical characterization of the I/O coupler performance, we used HFSS to simulate a back-to-back connection between the I/O couplers as seen in Fig. 5.1. For the purpose of this simulation, the dielectric parts of the coupler were made with Rexolite polystyrene due to its low refractive index, $n = 1.58$ and because it is the same material used for the rods in the LIC PhC. The metallic parts of the coupler were simulated with PEC (perfect electric conductor) material.

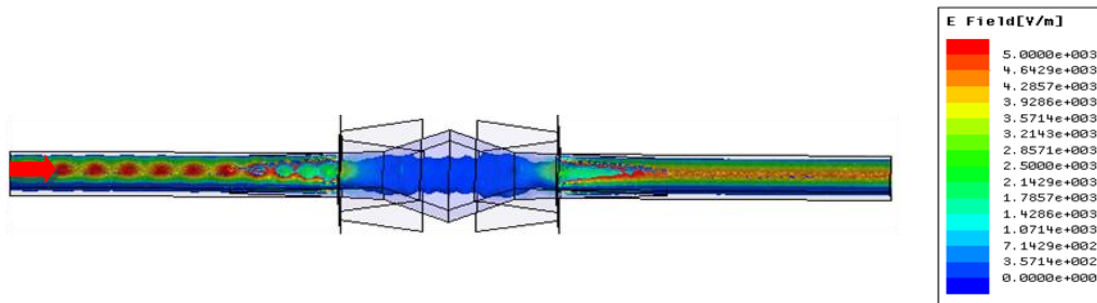


Figure 5.1 Electric field distribution for I/O couplers at 12 GHz.

Also in Fig. 5.1, we can see the electric field distribution through the couplers, which provides a qualitative notion of the confinement of light between the couplers. This electric field distribution shows efficient coupling since the fields are completely confined within the couplers, with virtually no diverging fields in the vertical or horizontal planes. This coupling efficiency is confirmed quantitatively in Fig. 5.2, which presents the numerical results for the insertion loss between the I/O couplers. This numerical results yield an insertion loss lower than -0.6 dB for 8 – 12.4 GHz.

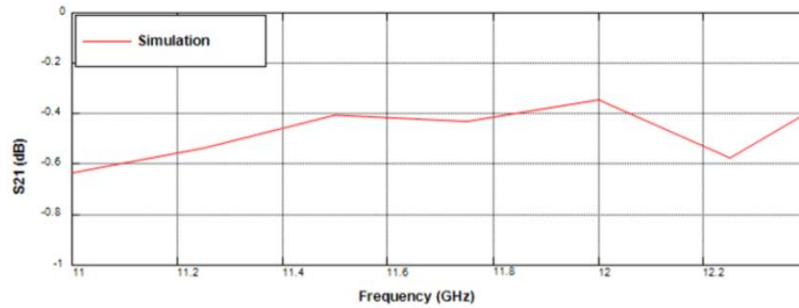


Figure 5.2 Numerical results for back-to-back I/O couplers.

5.4 Fabrication of I/O Coupler

Given the satisfactory numerical results, we fabricated the dielectric transitions with Rexolite polystyrene ($\epsilon = 2.586 - j0.01484$) and the tapered flanges with aluminum, both using an automated milling machine. The vertically taper of the transition was achieved by placing a rectangular Rexolite slab on a 7 degree angle and milling the opposite side of the slab and then turning it and repeating on the other side. Similarly, the horizontal taper on each side of the dielectric horn was milled to an angle of 40 degrees. The tapered aluminum flanges were milled to form a 45 degree angle around the dielectric horn. Figure 5.2 shows the two dielectric transitions of our I/O couplers. The complete I/O coupler is shown in Fig. 5.3, including the coaxial-to-waveguide transition, a WR90 waveguide, a tapered dielectric line and dielectric horn, and two metallic flanges.

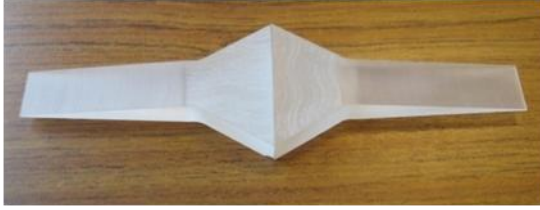


Figure 5.3 Dielectric transitions.



Figure 5.4 Fabricated I/O coupler.

5.5 Experimental Verification of Coupler Efficiency

To verify the numerical results shown in Fig. 5.2, we prepared a microwave measurement setup that included an Agilent 8722B network analyzer, two sets of 3.5 mm coaxial cables, and the two I/O couplers that we fabricated. We then performed the necessary calibration of the network analyzer using “Open-Short-Load” standards and a TRL method to guarantee the accuracy of our measurements [18, 19]. The couplers were setup as in the simulation shown in Fig. 5.1 in order to extract experimental data and compare it with numerical results. Figure 5.5 shows this comparison, where the experimental data shows that the insertion loss is lower than -1.2 dB for the measured frequency range. The experimental data also shows a good agreement with the numerical results with only a variation of about 0.6 dB.

The results from Fig. 5.5 are encouraging since they show an improvement of nearly 2 dB in the insertion loss compared any other equivalent coupler that we found in the literature; nevertheless, there is another component to the coupling loss when connecting these I/O couplers with the PhC slab as shown in Fig. 5.6. The data measured in the previous experiment is component (1), which is the insertion loss for the transition from the coaxial medium through the rectangular

waveguide to the dielectric waveguide. The other component of the coupling loss is (2) in Fig. 5.6, the insertion loss from the tapered dielectric waveguide to the 2D PhC waveguide. In order to measure this dielectric-waveguide-to-PhC (DWP) coupling loss (2), we had to isolate it from the other two sources of power loss in our microwave communications system: the coaxial-to-dielectric-waveguide (CDW) coupling loss (1) and the SCPPhC propagation loss (3).

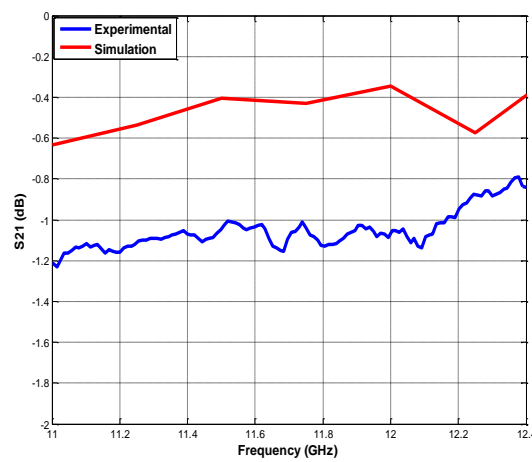


Figure 5.5 Comparison of experimental and numerical results for back-to-back I/O couplers.

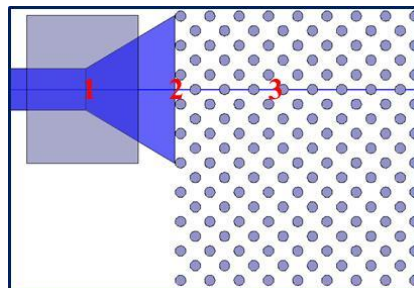


Figure 5.6 Graphical notion of transmission loss components.

The CDW coupling loss component is nullified trivially by calibrating it out of the experiment, i.e., the I/O couplers are connected back to back and the resulting measurement is used as the starting condition for the next measurement. There is no standard method to nullify the SCPhC propagation loss from our measurement; thus we devised a technique to isolate the DWP coupling loss from the measurement of the insertion loss through both components. We achieved this by measuring the insertion loss for PhC slabs of different length and taking a single frequency data point for each length to plot a linear extrapolation of the data as shown in Fig. 5.7 (a) for LIC PhCs and in Fig 5.7 (b) for HIC PhCs. The value of the extrapolated line when it intersects the Y axis is equivalent to the DWP coupling loss since it represents the insertion loss between the two I/O couplers through a PhC of infinitesimal length.

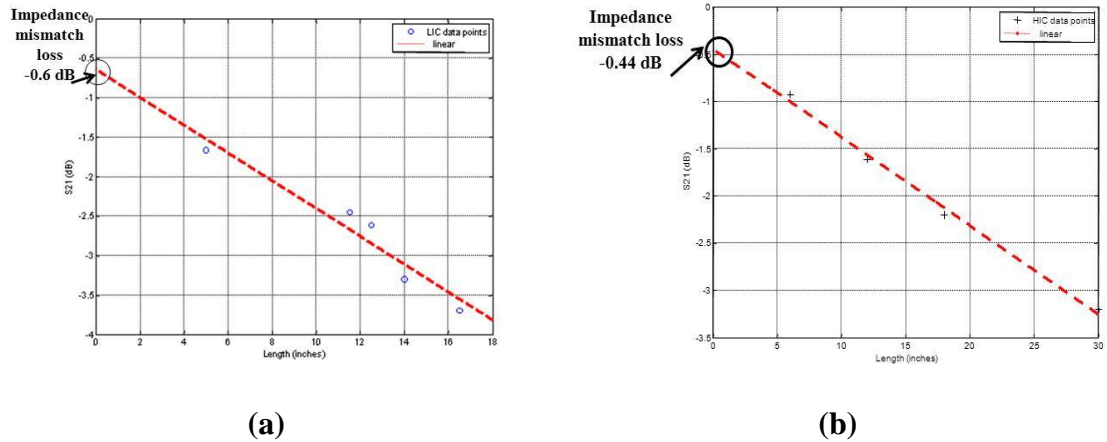


Figure 5.7 Impedance mismatch loss calculation through linear extrapolation of the transmission data for different-length PhCs, (a) for LIC PhC, and (b) for HIC PhC.

We found that the DWP coupling loss for LIC PhC is -0.6 dB and -0.44 dB for the HIC PhC. Given these findings, we were able to determine the total coupling loss by adding the CDW and DWP coupling loss components; thus, for the LIC PhC the total coupling loss is -1.8 dB or unilaterally -0.9 dB. For the HIC PhC, the total coupling is -1.66 dB or -0.83 dB at each coupler.

Chapter 6

CONCLUSIONS AND FUTURE WORK

6.1 Conclusions

In this research, we investigated and experimentally demonstrated novel dispersion properties of dispersion-engineered photonic crystals (PhCs). In particular, this research focused on the self-collimation effect in PhCs. In addition, in Chapter 5 we addressed the issue of coupling the PhC to a coaxial medium with the design and fabrication of a hybrid coupling structure. This research was conducted with the purpose of realizing a dielectric waveguiding mechanism based on a self-collimating PhC structures that would provide a transmission efficiency comparable to the established waveguiding technologies in the microwave frequency regime. Following this goal, we carried out this research systematically starting with the design and fabrication of a low-index-contrast (LIC) PhC and advancing to a more efficient high-index-contrast (HIC) PhC.

We can draw the following conclusions from the work conducted in this research: (1) Self-collimation can be demonstrated even in low-index-contrast PhCs, but the confinement of light through this dispersion effect is more efficient for high-index-contrast PhCs. (2) Our coaxial-to-PhC coupling mechanism can serve as model for the integration of PhC structures in microwave communications systems. (3) The significance of this research is supported by the fact that the experimental results that we presented for the transmission efficiencies of our PhC designs are among the best

that have been reported for PhC guiding mechanisms in the microwave frequency regime. (4) These results approach the efficiencies required for practical applications in the field. Although some improvements are still necessary and possible, with this research we have laid a path that could certainly lead to a competitive waveguiding scheme.

6.2 Future Work

Our most recent research has demonstrated that significant improvements are still possible for the coax-to-PhC coupling structures. Figure 6.1 depicts renderings for two of the proposed methods to improve impedance matching between these couplers and PhCs. The illustration in Fig 6.1(a) suggests that by optimizing the dimensions of the dielectric horn in our coupler we can improve the impedance matching with PhCs made of different materials. The design depicted in Fig. 6.1(b) proposes what we like to call an effective index coupler, which can be realized by drilling an aperiodic arrangement of holes with the shape of a lens in the horn of the coupler with the intention of reducing the divergence of light exiting the coupler.

We have also contemplated improving the PhC structure. If the homogeneity of the structure is not a requirement, it is possible to design a hybrid PhC lattice with photonic bandgap (PBG) material surrounding a self-collimating PhC. This would be similar to a line defect in a PBG, except that in-plane light would propagate through the SCPhC and any divergence of fields would be suppressed by the PBG. This hybrid design could be realized with a structure similar to the HIC PhC presented in Chapter 4 of this thesis.

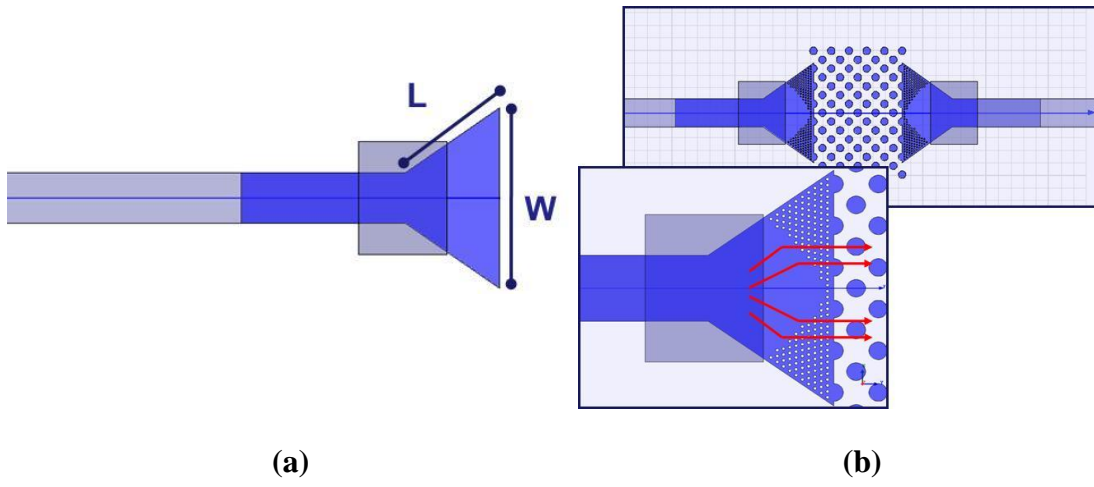


Figure 6.1 Illustrations of proposed methods to improve impedance matching between I/O couplers and PhCs (a) by optimizing the dimensions of the dielectric horn, and (b) by designing an effective index coupler.

REFERENCES

- [1] Mohammed, E. and et al, "Optical interconnect system integration for ultra-short reach applications," Intel Technology Journal, vol. 8, 115 (2004).
- [2] Joannopoulos, J. D., Johnson, S. G., Winn J. N., and Meade R. D.,(1995) [Photonic Crystals: Molding the Flow of Light], 2nd Ed., Princeton University Press, Princeton (2007).
- [3] Prather, D. W., Shi, S., Sharkawy, A., Murakowski, J., and Schneider, G., [Photonic Crystals: Theory, Applications, and Fabrication], John Wiley & Sons, Hoboken, NJ, 197-214 (2009).
- [4] Yablonovitch, E., "Inhibited spontaneous emission in solid-state physics and electronics," Phys. Rev. Lett. 58, 2059-2062 (1987).
- [5] John, S., "Strong localization of photons in certain disordered dielectric superlattices," Phys. Rev. Lett. 58, 2486-2489 (1987).
- [6] Ho, K. M., Chan, C. T., and Soukoulis, C. M., "Existence of a photonic gap in periodic dielectric structures," Phys. Rev. Lett. 65, 3152-3155 (1990).
- [7] Lu, Z., Schuetz, C. A., Shi, S., Chen, C., Behrmann, G. P., and Prather, D. W., "Experimental demonstration of self-collimation in low index contrast photonic crystals in the millimeter wave regime," *IEEE Transactions on Microwave Theory and Techniques*, 53, 1362-1368 (2005).
- [8] Prather, D. W., Shi, S., Murakowski, J., Schneider, G., Sharkawy, A., and Chen, C., " Photonic crystal structures and applications: Perspective, overview, and development," *IEEE Journal on Selected Topics in Quantum Electronics*, 12, 1416-1436 (2006).
- [9] Chen, C., Sharkawy, A., Shi, S., and Prather, D. W., "Integrated Photonics Research", OSA Technical Digest, 39 (2003).

- [10] Noda, S., Chutinan, A., and Imada, M., "Trapping and emission of photons by a single defect in a photonic bandgap structure," *Nature*, 407, 608-610 (2000).
- [11] Sharkawy, A., Pustai, D., Shi, S., and Prather, D. W., "High transmission through waveguide bends by use of polycrystalline photonic crystal structures," *Opt. Lett.*, 28, 1197-1199 (2003).
- [12] Prather, D. W., Shi, S., Murakowski, J., Schneider, G., Sharkawy, A., Chen, C., Miao, B., and Martin, R., "Self-collimation in photonic crystal structures: A new paradigm for applications and device development," *Journal of Physics D: Applied Physics*, 40, 2635-2651(2007).
- [13] Lu, Z., Murakowski, J. A., Schuetz, C. A., Shi, S., Schneider, G. J., Samluk, J. P., and Prather, D. W., "Perfect lens makes a perfect trap," *Optics Express* 14, 6, 2228-2235 (2006).
- [14] Yablonovitch, E., "Photonic crystals," *J. Mod. Opt.* 41, 173–194 (1994).
- [15] Sabas, J. N., Mirza, I. O., Shi, S., and Prather, D. W., "An efficient self-collimating photonic crystal coupling technique in the RF regime," *Proc. SPIE* 7609, 76090M (2010).
- [16] Tehrani, H., Li, M-Y., and Chang, K., "Broadband microstrip to dielectric image line transitions," *IEEE MW and Guided Wave Letters*, 10(10), 409-411 (2000).
- [17] Sano, K., and Yoneyama, T., "A transition from microstrip to dielectric-filled rectangular waveguide in surface mounting," *IEEE MTT-S Digest*, 2, 813-816 (2002).
- [18] Mirza, I. O., Shi, S., and Prather, D. W., "Phase Modulation Using Dual Split Ring Resonators," *Opt. Express* 17, 5089-5097 (2009).
- [19] Mirza, I. O., Sabas, J. N., Shi, S., and Prather, D. W., "Experimental demonstration of metamaterial-based phase modulation," *Proc. Progress In Electromagnetics Research, PIER* 93, 1-12 (2009).